

# RAPID SOLIDIFICATION OF SN-CU-AL ALLOYS FOR HIGH RELIABILITY LEAD-FREE SOLDER: PART I. MICROSTRUCTURAL CHARACTERIZATION OF RAPIDLY SOLIDIFIED SOLDERS

KATHLENE N. REEVE\*<sup>1,4</sup>, STEPHANIE M. CHOQUETTE<sup>2,3,5</sup>, IVER E. ANDERSON<sup>2,3,6</sup>,  
AND CAROL A. HANDWERKER<sup>1,7</sup>

1. – Purdue University, 701 West Stadium Ave., West Lafayette, IN, 47907, USA. 2. – Ames Laboratory (USDOE), Iowa State University, Ames, IA, 50011, USA. 3. – Iowa State University, Ames, IA, 50011, USA. 4. – tel.: +1-816-824-4851, fax: +1-765-494-1204, email: klindley@purdue.edu. 5. – email: smc1@iastate.edu. 6. – email: andersoni@ameslab.gov. 7. – email: handwerker@purdue.edu.

\* Corresponding author: K. N. Reeve

## Abstract:

Particles of  $\text{Cu}_x\text{Al}_y$  in Sn-Cu-Al solders have previously been shown to nucleate the  $\text{Cu}_6\text{Sn}_5$  phase during solidification. In this study, the number and size of  $\text{Cu}_6\text{Sn}_5$  nucleation sites was controlled through the particle size refinement of  $\text{Cu}_x\text{Al}_y$  via rapid solidification processing and controlled cooling in a differential scanning calorimeter. Cooling rates spanning eight orders of magnitude were used to refine the average  $\text{Cu}_x\text{Al}_y$  and  $\text{Cu}_6\text{Sn}_5$  particle sizes down to sub-micron ranges. The average particle sizes, particle size distributions, and morphologies in the microstructures were analyzed as a function of alloy composition and cooling rate. Deep etching of the samples revealed the three dimensional microstructures and illuminated the epitaxial and morphological relationships between the  $\text{Cu}_x\text{Al}_y$  and  $\text{Cu}_6\text{Sn}_5$  phases. Transitions in the  $\text{Cu}_6\text{Sn}_5$  particle morphologies from faceted rods to non-faceted, equiaxed particles was observed both as a function of cooling rate and composition. Initial solidification cooling rates within the range of  $10^3$  °C/s -  $10^4$  °C/s were found to be optimal for realizing particle size refinement and maintaining the  $\text{Cu}_x\text{Al}_y/\text{Cu}_6\text{Sn}_5$  nucleant relationship. In addition, little evidence of the formation or decomposition of the ternary- $\beta$  phase in the solidified alloys was noted. Solidification pathways omitting the formation of the ternary- $\beta$  phase agreed well with observed room temperature microstructures.

**Key words:** intermetallics; rapid-solidification, quenching; microstructure; metallography; scanning electron microscopy, SEM.

## 1. INTRODUCTION

Aluminum micro-alloying additions have been shown to affect the solidification and microstructure of Pb-free solder alloys, particularly in Sn-Ag-Cu and Sn-Cu solder alloys, by reducing solder undercooling, eliminating or reducing the  $\text{Ag}_3\text{Sn}$  intermetallic compound (IMC) plate morphology, and forming  $\text{Cu}_x\text{Al}_y$  IMCs. [1–6] To form solder joints, solder alloys are commonly converted into powder particles, incorporated into a solder paste, and melted and solidified in final assembly to connect components to circuit boards. In the context of designing Sn-Cu-Al solder joint alloys, it is important to establish what the optimal  $\text{Cu}_x\text{Al}_y$  microstructures should be in both the as-fabricated powder and after soldering of the components is completed. Design factors that must be considered include:

1. the role of solidification cooling rate and alloy composition on the formation, morphologies, and size distributions of  $\text{Cu}_x\text{Al}_y$  particles,
2. the ability of  $\text{Cu}_x\text{Al}_y$  to serve as a heterogeneous nucleation catalyst for the  $\text{Cu}_6\text{Sn}_5$  IMC phase, and the resulting morphologies and sizes of the  $\text{Cu}_6\text{Sn}_5$ , and
3. the possible presence of the ternary- $\beta$  phase during Sn-Cu-Al alloy solidification and its subsequent decomposition at low temperatures, as predicted by thermodynamics calculations, and its possible effect on  $\text{Cu}_6\text{Sn}_5$  nucleation. [2,5,6]

Reeve et al. confirmed the initial formation of the  $\text{Cu}_x\text{Al}_y$  phases in the temperature ranges of 723K - 823K (450°C - 550°C) for seven different Sn-Ag-Cu-Al alloys and two different Sn-Cu-Al alloys. [2] The observation of this high solidification temperature provides the possibility of  $\text{Cu}_x\text{Al}_y$  IMC particles serving as persistent heterogeneous nucleation catalysts for the  $\text{Cu}_6\text{Sn}_5$  phase, where “persistence” is defined as having minimal coarsening after multiple solder reflow cycles to a maximum temperature of 523K (250°C), as typically required for circuit board assembly. Xian et al. observed  $\text{Cu}_6\text{Sn}_5$  formation on  $\text{Cu}_x\text{Al}_y$  particles within Sn-4.0Cu-xAl and Sn-0.7Cu-0.05Al wt. % alloys, and identified the orientation relationship between the two IMC phases. [5,6]

$$(\bar{1}\bar{2}10)_{\text{Cu}_6\text{Sn}_5} \parallel (10\bar{1})_{\text{Cu}_x\text{Al}_y} \text{ and } [0001]_{\text{Cu}_6\text{Sn}_5} \parallel [111]_{\text{Cu}_x\text{Al}_y}$$

Xian et al. determined that for a Sn-4.0Cu-0.2Al wt. % alloy, the nucleation undercooling for the  $\text{Cu}_6\text{Sn}_5$  IMC was reduced from 7.8 to 3.6 K and the number of  $\text{Cu}_6\text{Sn}_5$  IMC grains per unit area increased by a factor of eight, as dictated by the number of  $\text{Cu}_x\text{Al}_y$  particles. [5] More recently, Xian et al. have shown the influence of dilute additions of Al on the formation of  $\text{Cu}_6\text{Sn}_5$  in a Sn-0.7Cu-0.05Al wt. % alloy, where they noted that the number of primary  $\text{Cu}_6\text{Sn}_5$  rose by a factor of seven, while the length of (rod-like)  $\text{Cu}_6\text{Sn}_5$  particles was reduced by a factor of four, compared with a Sn-0.7Cu wt. % alloy. [6]

Some of the earliest assessments of the Cu-rich IMCs within the Cu-Al binary system were presented by Smith et al. [7] and Wasserman [8]. An extensive review of the system and an updated binary phase diagram was given by Murray [9] and subsequently modified by Liu et al. [10] and Okamoto [11]. The most recent update to the Cu-Al binary was made by Ponweiser et al. in 2011. [12] Notable shifts in phase fields were made for several Cu-rich IMCs, where the similarities between the crystal structures of  $\text{Cu}_{33}\text{Al}_{17}$  ( $\delta$ ) and  $\text{Cu}_9\text{Al}_4$  ( $\gamma$ ) phases and the narrowing of the two-phase field between these two phases was analyzed. [12] Recent revisions have also been made to the Cu-Sn binary system, particularly in reference to the high temperature Cu-rich IMC  $\beta$  phase. [13,14]

In the ternary Sn-Cu-Al system, the phase diagram is incomplete. The similarities between the crystal structures and probable ranges of stoichiometry of the IMCs, the numerous morphological and compositional changes seen during the predicted ternary- $\beta$  phase decomposition for multiple alloys, and the presence of a liquid-liquid miscibility gap have led to several plausible phase diagrams being proposed, but inconsistencies remain. [15–18] In a recent study, Chakrabarty and Jacob analyzed formation, stability, and decomposition of Cu-rich Sn-Cu-Al ternary alloys, observing the formation of  $\alpha$ ,  $\beta$ ,  $\gamma$ , and the ordered  $\beta_1$  ternary phases after long-term isothermal annealing of alloys between 773K (500°C) and 823K (550°C). [16,17] These results, as well as results from Reeve et al. on Sn-rich alloys [2], indicate that the alloy composition, the alloy liquid equilibration temperature (above or below the liquidus) before cooling begins, and the solidification path of the alloy are all extremely important factors in terms of the resulting room temperature solidification microstructure and the presence of ternary IMC phases within these Sn-Cu-Al alloys.

One of the questions remaining for Sn-rich Sn-Cu-Al ternary alloys is whether or not the formation and subsequent solid-state decomposition of the ternary- $\beta$  actually occurs, or if the ternary- $\beta$  phase is, in fact, unstable, contrary to the current thermodynamic predictions. Figure 1 displays the distinctly different types of solidification paths predicted for three different alloy compositions, with and without the formation of the ternary- $\beta$  phase, and Fig. 2 shows the computed Sn-Cu-Al ternary liquidus projection from the Sn-rich corner, such that the IMC transitions can be viewed. [18] The presence, or absence, of the ternary- $\beta$  phase during solidification of these alloys has a notable effect on the stability and formation of other IMC phases within the system. The room temperature stable phases within all of the compositions when the ternary- $\beta$  phase is present during solidification are  $\beta$ -Sn,  $\text{Cu}_9\text{Al}_4$  ( $\gamma_1$ ), and  $\text{Cu}_6\text{Sn}_5$  ( $\eta'$ ) (Fig. 1a-c). When the ternary- $\beta$  is omitted in the solidification predictions (Fig. 1d-f), the room temperature stable phases within all three alloys become  $\beta$ -Sn,  $\text{Cu}_{33}\text{Al}_{17}$  ( $\delta$ ), and  $\text{Cu}_6\text{Sn}_5$  ( $\eta'$ ). Additionally, the omission of the ternary- $\beta$  phase from the solidification predictions has a major effect on the temperature stability and formation of  $\text{Cu}_6\text{Sn}_5$  within all of the alloys. In all cases, suppression of the ternary- $\beta$  phase increases the temperature stability of  $\text{Cu}_6\text{Sn}_5$  through the formation of the hexagonal, high-temperature  $\text{Cu}_6\text{Sn}_5$  ( $\eta$ ) phase. Additionally, when the ternary- $\beta$  phase formation is suppressed, as seen in Fig. 1d-f, a variation in temperature stability of the  $\text{Cu}_6\text{Sn}_5$  formation, in reference to the typical solder reflow processing temperature of 523K (250°C) used during microelectronics fabrication, can be seen. Composition #1 (Fig. 1d) displayed formation of  $\text{Cu}_6\text{Sn}_5$  ( $\eta$ ) directly at the ternary eutectic transition (500K (227°C)), composition #2 (Fig. 1e) displayed proeutectic formation of  $\text{Cu}_6\text{Sn}_5$  ( $\eta$ ) at ~513K (~240°C) (below the 523K (250°C) solder reflow processing temperature), and composition #3 (Fig. 1f) displayed proeutectic formation of the  $\text{Cu}_6\text{Sn}_5$  ( $\eta$ ) at ~540K (~267°C) (above the 523K (250°C) solder reflow processing temperature). Therefore, the formation of the ternary- $\beta$  phase, although not stable at room temperature, has a notable influence over the predicted microstructure of the alloys and the temperature stability of the resulting phases.

In this paper we have used these three compositions to investigate the high temperature stability and morphologies of the  $\text{Cu}_x\text{Al}_y$  phases as a function of composition and cooling rate, the nucleant

relationship with  $\text{Cu}_6\text{Sn}_5$ , and the possible presence of the ternary- $\beta$  phase during solidification via rapid solidification and controlled differential scanning calorimetric (DSC) cooling. The ability to dictate the formation, size, and size distribution of both the  $\text{Cu}_x\text{Al}_y$  and, subsequently, the  $\text{Cu}_6\text{Sn}_5$  phase, has the potential to not only improve solder joint uniformity, but to also improve solder joint mechanical performance and fatigue tolerance. Xian et al. noted that the combination of constitutional supercooling in the liquid and the potent  $\text{Cu}_x\text{Al}_y$  nuclei resulted in the nucleation of  $\text{Cu}_6\text{Sn}_5$  at a number density that was likely dependent upon the size and distribution of the  $\text{Cu}_x\text{Al}_y$  IMC particles within the system. [5] In this paper, these ideas have been tested by controlling the  $\text{Cu}_x\text{Al}_y$  and  $\text{Cu}_6\text{Sn}_5$  phases through variations in composition and solidification cooling rate, from slow cooling to rapid solidification processing (RSP) and melt spinning. The resulting microstructures are analyzed in regard to both IMC phases present ( $\text{Cu}_x\text{Al}_y$  and  $\text{Cu}_6\text{Sn}_5$ ), the resulting morphologies, the relative association between the IMC, and the resulting IMC particle sizes, coarsening rates of the IMC, and shifts in particle size distributions across the chosen cooling rate regimes.

## 2. EXPERIMENTAL VARIABLES AND PROCEDURES

Three different Sn-Cu-Al alloy compositions and four distinct cooling rate regimes resulted in estimated cooling rates that span eight orders of magnitude for Part I of this study. Table I outlines the cooling methods, the estimated cooling rates for each method, the alloy compositions of the samples used within each cooling method, and all of the collected and calculated particle data for the  $\text{Cu}_x\text{Al}_y$  and  $\text{Cu}_6\text{Sn}_5$  phases. (Note that the average IMC compositions, and hence, dominant  $\text{Cu}_x\text{Al}_y$  phase ( $\text{Cu}_{33}\text{Al}_{17}$  vs.  $\text{Cu}_9\text{Al}_4$ ), was determined by energy dispersive spectroscopy (EDS), as described below.) Three alloy compositions were studied: #1 - Sn-2.29Cu-0.86Al at. % (Sn-1.25Cu-0.2Al wt. %), #2 - Sn-2.59Cu-0.43Al at. % (Sn-1.41Cu-0.1Al wt. %), and #3 - Sn-5.39Cu-1.69Al at. % (Sn-3.0Cu-0.4Al wt. %). These alloys allowed comparison of the effects of (1) different theoretical (maximum) volume fractions of the  $\text{Cu}_x\text{Al}_y$  and  $\text{Cu}_6\text{Sn}_5$  IMC phases at room temperature, (2) different solidification pathways with respect to formation of the ternary- $\beta$  IMC and  $\text{Cu}_6\text{Sn}_5$  phases as predicted from thermodynamic calculations, and (3) different cooling

rates on morphologies and spatial relationships between the various IMCs as they formed. Four cooling methods were chosen to study the effects of alloy cooling rate from a common superheat temperature of 1473K (1200°C) on the solder IMC microstructure: controlled DSC cooling at the four different cooling rates of 0.017 °C/s (1 °C/min), 0.17 °C/s (10 °C/min), 0.83 °C/s (50 °C/min), and 1.65 °C/s (99 °C/min); ice water quenching (WQ) (estimated cooling rate of  $10^3$  °C/s); drip atomization (DA) of 260 µm diameter spheres (estimated cooling rate of  $10^4$  °C/s); and melt spinning at two different wheel speeds, 5 m/s and 25 m/s, (estimated cooling rates of  $10^5$  and  $10^6$  °C/s, respectively). The common superheat temperature of 1473K (1200°C) was chosen specifically to ensure solidification from a homogeneous alloy liquid, as it was previously shown by Reeve et al. that variations in superheat temperature (1473K vs. 1073K (1200°C vs. 800°C)) can have a notable effect on the as-solidified  $\text{Cu}_x\text{Al}_y$  particle size. [2] All of the as-solidified solder samples were then analyzed via scanning electron microscopy (SEM). It must be noted that measuring of solidification rates for specific RSP methods is still an area of debate within the field. [19] Accurately measuring the temperature of a rapidly cooled melt, estimating the heat transfer coefficients for various heat sinks, and assessing the nucleation temperature of an alloy all present difficulties for the determination of rapid solidification rates. Due to these well-known issues, the authors have assigned cooling rates to specific RSP methods based on conventional order-of-magnitude estimates.

## 2.1 DSC CONTROLLED COOLING

The DSC cooled samples were prepared from elemental Sn, Cu, and Al of 99.99% purity at the Materials Preparation Center (MPC) of Ames Laboratory<sup>1</sup>. The original alloy casting from which the DSC samples were prepared was made via the same procedure as described in section 2.2 for the WQ samples, with length of wire (1.7 mm diameter) drawn from the WQ ingot. A 100 mg sample was cut from the wire for each DSC slow cooling rate experiment. The DSC employed was a Pegasus heat flux DSC 404C by Netzch. Each sample was placed in an alumina crucible, continually flushed with nitrogen, and heated to a superheat of 1473K (1200°C) at 20 °C/min (0.33 °C/s). Each sample was held at the 1473K (1200°C)

---

<sup>1</sup> <http://www.ameslab.gov/mpc> - Ames Laboratory Materials Preparation Center, Ames, IA, USA.

superheat temperature for 10 min and cooled at the specified cooling rates of either 0.017 °C/s, 0.17 °C/s, 0.83 °C/s, or 1.65 °C/s. Two alloy samples (~100 mg) were run through the DSC slow cooling rate procedure per cooling rate. Each sample cross-section was then analyzed, resulting in two cross-sections examined per the four different cooling rate procedures. Figure 1d shows the predicted solidification path for the Sn-2.29Cu-0.86Al at. % alloy (composition #1) chosen for the DSC cooled samples. The room temperature microstructure was predicted to be composed of three phases,  $\beta$ -Sn + Cu<sub>6</sub>Sn<sub>5</sub> ( $\eta'$ ) + Cu<sub>33</sub>Al<sub>17</sub> ( $\delta$ ).

## 2.2 ICE WATER QUENCHING

The WQ samples were prepared from elemental Sn, Cu, and Al of 99.99% purity at the Materials Preparation Center (MPC) of Ames Laboratory<sup>2</sup>. The castings were made as 100g samples, sealed in quartz tubes under an argon atmosphere, superheated at 1473K (1200°C) for 60 min (with periodic agitation), and finally quenched into an ice water bath with no fracture of the quartz tube ampule. The solder ingots were then drawn into 1.7 mm diameter wires, from which the samples were cut for microstructural examination. Wire drawing was used to homogenize the microstructure. One longitudinal wire cross-section (~ 2 cm long) and one transverse wire cross-section (0.17 cm) were characterized for each of the two different WQ sample compositions (Sn-2.29Cu-0.86Al and Sn-5.39Cu-1.69Al at. %) shown in Table I. Figure 1d and 1f display the predicted solidification paths for the Sn-2.29Cu-0.86Al at. % (composition #1) and Sn-5.39Cu-1.69Al at. % (composition #3) alloys chosen for the WQ cooled samples. The room temperature microstructures were predicted to be composed of three phases,  $\beta$ -Sn + Cu<sub>6</sub>Sn<sub>5</sub> ( $\eta'$ ) + Cu<sub>33</sub>Al<sub>17</sub> ( $\delta$ ).

## 2.3 DRIP ATOMIZATION

The target composition of the DA ball grid array (BGA) spheres was Sn-2.59Cu-0.43Al at. % (Sn-1.41Cu-0.10Al wt. %). To produce the desired alloy composition, the following masses were added to an Ar-filled graphite crucible: 984.9g of elemental Sn, 7.1g of elemental Cu, and 8.0g of a Cu-Al master alloy,

---

<sup>2</sup> <http://www.ameslab.gov/mpc> - Ames Laboratory Materials Preparation Center, Ames, IA, USA.

with a final composition targeted to produce  $\text{Cu}_{33}\text{Al}_{17}$  ( $\delta$ ) IMC in a Sn-Cu alloy. To initially alloy the added materials, the crucible was heated to 1073K (800°C) and held for 15 minutes. The temperature of the crucible was then increased to 1473K (1200°C) and held for 10 minutes. The alloyed liquid was DA processed with a proprietary system (Fukuda Co.) that used a pulsating plunger to force the alloy melt through an orifice plate, resulting in 260 $\mu\text{m}$  diameter spheres. The spheres were cooled and solidified during free-fall in an inert argon gas chamber. Clogging of the crucible occurred prematurely after 10 minutes of atomization, yielding a final efficiency of 0.2% of the starting alloyed melt. The drip atomization was performed by Fukuda Co. in Japan<sup>3</sup>, facilitated by Nihon Superior<sup>4</sup>. Cross-sections of 10 different DA spheres were characterized by SEM/EDS analysis of the alloy. Figure 1e shows the predicted solidification path for the Sn-2.59Cu-0.43Al at. % alloy (composition #2) chosen for the drip atomization. The room temperature microstructure was predicted to be composed of three phases,  $\beta\text{-Sn} + \text{Cu}_6\text{Sn}_5$  ( $\eta'$ ) +  $\text{Cu}_{33}\text{Al}_{17}$  ( $\delta$ )

#### 2.4 MELT SPINNING

Two melt spun ribbon (MSR) alloy castings were produced via the melt spinning operation, both with a target composition #3. The melt-spinner, located at Ames Laboratory, was housed in a custom stainless steel vacuum chamber. The rotating chill block that acted as the heat sink for the alloy melt during the RSP was made of oxygen-free high-conductivity (OFHC) copper. The chill block was rotated at chill surface speeds of 5 m/s and 25 m/s in order to produce two different cooling rates for the two separate cast ribbons. Differential pressure for melt ejection was measured by means of a differential pressure manometer and was set at 105 torr (~2psi). The crucible material that held the alloy melt was a  $\text{SiO}_2$  (quartz glass) with an outer diameter of 15 mm. The orifice diameter of the crucible was 0.8 mm and was formed by use of an embedded quartz precision capillary. The heating of the alloy was performed with a Pillar 15kW 450 kHz induction generator and during casting each melt was superheated to 1473K (1200°C), as monitored by a

---

<sup>3</sup> <http://www.fukuda-kyoto.co.jp/01info-e/f-kyoten.html> - Fukuda Metal Foil and Powder Co., Yamashina-ku, Kyoto, Japan.

<sup>4</sup> <http://www.nihonsuperior.co.jp/english/> - Nihon Superior, Esaka-Cho, Suita City, Osaka, Japan.



2-color pyrometer. Upon release of the molten alloy and impingement with the rotating copper chill block, rapidly solidified cast ribbons were formed. Estimated cooling rates for the two alloy cast ribbons were approximated to be  $10^5$  °C/s for the 5 m/s chill block wheel speed and  $10^6$  °C/s for the 25 m/s wheel speed. Longitudinal cross-sections of the ribbons (~ 2 cm long) were used for SEM analysis for each of the two different cool rate samples. Figure 1f shows the predicted solidification path for composition #3, chosen for the MSR samples. The room temperature microstructure is predicted to be composed of three phases,  $\beta$ -Sn +  $\text{Cu}_6\text{Sn}_5$  ( $\eta'$ ) +  $\text{Cu}_{33}\text{Al}_{17}$  ( $\delta$ ).

## 2.5 METALLOGRAPHY, SEM, AND PARTICLE ANALYSIS

For microstructural analysis after each cooling rate treatment the samples were metallographically cross-sectioned and analyzed via SEM. The solder samples were mounted individually in a cold mount epoxy/resin and cured for 24 hours at room temperature. The sample surfaces were polished via a standard metallographic grinding and polishing sequence of: 400/600/800/1200 grit SiC paper with water as a lubricant, followed by 1/0.5/0.25/0.05  $\mu\text{m}$  diamond/glycol polishing suspension on high matte polishing pads (used specifically for soft metallic materials) with RedLube<sup>TM</sup> lubricant obtained from Allied High Tech Products Inc<sup>5</sup>. In addition to the standard metallographic sample preparations and two dimensional (2-D) microstructural analysis via SEM, the WQ samples, DA sample, and MSR samples were deep etched and analyzed via SEM. The deep etching procedure employed was identical to the procedure outlined in reference [20] and was used to etch away the  $\beta$ -Sn matrix phase for three dimensional (3-D) examination of the IMC morphologies present in the samples.

SEM images for the DSC cooled samples and for the WQ samples were obtained in backscatter electron (BSE) mode at 20keV on a Hitachi S-2460N SEM. SEM images for the WQ, DA, and MSR samples were gathered in BSE mode at 15keV on a NanoScience Phenom Desktop -  $\text{CeB}_6$  filament SEM. SEM images for the deep etched DA sample were gathered in secondary electron (SE) mode at 5 keV on a FEI Quanta-250 Field Emission SEM at Iowa State University's Materials Analysis and Research

---

<sup>5</sup> <http://alliedhightech.com/> - Allied High Tech Products Inc, Rancho Dominguez, CA, USA.

Laboratory (MARL) microscopy facility<sup>6</sup>. SEM images for deep etched WQ and MSR samples were obtained in both BSE and SE modes at 10-20 keV on a FEI Quanta 3-D Field Emission Dual-beam SEM at the Purdue Life Science Microscopy Facility (LSMF)<sup>7</sup>. Finally, quantitative metallographic analysis was performed on the images with the use of ImageJ photo analysis software, freely available from NIH<sup>8</sup>. Particle size diameters, particle size distributions, and volume fractions for the  $\text{Cu}_x\text{Al}_y$  and  $\text{Cu}_6\text{Sn}_5$  phases were measured via use of the ImageJ software particle analysis toolkit. Measurements via EDS were made throughout the analysis of all of the samples when the measurements could be reliably made on the  $\text{Cu}_x\text{Al}_y$  and  $\text{Cu}_6\text{Sn}_5$  IMC. Due to the extremely small particle size of the  $\text{Cu}_x\text{Al}_y$  IMC within the MSR samples, no EDS measurements could be accurately made and therefore no EDS data regarding the  $\text{Cu}_x\text{Al}_y$  phase within the two MSR samples is given within this study.

### 3. RESULTS AND DISCUSSION

In these experiments it was expected that IMC particle size would decrease with an increase in cooling rate. Additionally, it was predicted that one or both of the expected IMC phases,  $\text{Cu}_x\text{Al}_y$  and  $\text{Cu}_6\text{Sn}_5$ , within the system would exhibit morphological changes with variations in sample composition and cooling rate, possibly transitioning between faceted and non-faceted morphologies. Such refinement of IMC particle size and changes in IMC morphology with increases in cooling rate and with variations in alloy chemistry occur across many metallurgical systems. To the authors' knowledge, no work has previously reported these phenomena within a Pb-free solder system in which both  $\text{Cu}_x\text{Al}_y$  and  $\text{Cu}_6\text{Sn}_5$  IMC phases, given their identified nucleant relationship, were formed under the range of imposed solidification conditions. This section presents, a) how the  $\text{Cu}_x\text{Al}_y$  and  $\text{Cu}_6\text{Sn}_5$  IMC initially form under the influence of increasing cooling rate conditions, b) how the IMC particles interact under the various cooling rate conditions, and c) how the IMC particle formation and interaction is influenced by alloy composition. The microstructural data are analyzed below for each composition in terms of resulting  $\text{Cu}_x\text{Al}_y$  and  $\text{Cu}_6\text{Sn}_5$  IMC

---

<sup>6</sup> <http://www.marl.iastate.edu/FEISEM.html> - MARL, Iowa State University, Ames, IA, USA.

<sup>7</sup> <https://ag.purdue.edu/arp/Microscopy/Pages/default.aspx> - LSMF, Purdue University, West Lafayette, IN, USA.

<sup>8</sup> <http://www.nist.gov/lispix/doc/other-software/NIH-Image-notes.htm> - NIST NIH Image/Scion Image/ImageJ.

particle sizes, particle size distributions, compositions, morphologies, and degree of association between the two IMC phases. The results will then be summarized across the alloy compositions and cooling rate regimes in terms of overall IMC particle size refinement and the ideal solidification cooling rates for achieving simultaneous IMC particle size refinement and maintained preferred nucleation of  $\text{Cu}_6\text{Sn}_5$  from the  $\text{Cu}_x\text{Al}_y$  surfaces. Throughout the results it will be noted that there were very few IMC particles displaying possible ternary- $\beta$  phase decomposition. Thus, the solidification paths omitting the formation of the ternary- $\beta$  phase (Fig. 1d-f) will be used from this point forward to discuss the presented sample microstructures. It was the variation in  $\text{Cu}_6\text{Sn}_5$  temperature stability across the sample compositions that motivated the choice of the three Sn-Cu-Al alloys analyzed within this study (Fig. 1d-f, Table I). (Note that the difference in stability of the  $\text{Cu}_6\text{Sn}_5$  phase for these alloys will also be important during Part II of this study, where the coarsening of both IMC phases during solder reflow cycling is analyzed. [21])

### *3.1 DSC COOLING AND WQ SAMPLES – COMPOSITION #1 (Sn-2.29Cu-0.86Al at. %)*

Particle size and volume fraction data are shown in Table I. The DSC and WQ samples showed formation of both  $\text{Cu}_x\text{Al}_y$  and  $\text{Cu}_6\text{Sn}_5$  IMC with the average particle sizes showing a steady decrease in size with an increase in cooling rate. Undercooling within the DSC cooled samples ranged from 11 °C (0.017 °C/s cooling rate) to 8.5 °C (0.83 and 1.65 °C/s cooling rates). Undercooling for the WQ sample was recorded at approximately 8°C, after casting and subsequent reflow of the cast sample at 1473K (1200°C) in the DSC. [2] Representative micrographs of the Sn-2.29Cu-0.86Al at. % DSC and WQ samples can be seen in Fig. 3a-g. Compositional measurements made via EDS for both the  $\text{Cu}_x\text{Al}_y$  and  $\text{Cu}_6\text{Sn}_5$  phases are shown in Table II. The micrographs of the DSC cooled samples in Fig. 3a-d showed that all of the  $\text{Cu}_x\text{Al}_y$  particles were found along the outer edges of the as-solidified solder spheres. This was not observed for the  $\text{Cu}_6\text{Sn}_5$  particles, which were found within the bulk. In contrast to faster cooling rates, where the solidification front likely entrapped  $\text{Cu}_x\text{Al}_y$  particles, larger  $\text{Cu}_x\text{Al}_y$  particles were likely pushed ahead of the Sn solidification front in the DSC cooled samples and thus were found only along the outer edges of the solder spheres. Buoyancy differences between the  $\text{Cu}_x\text{Al}_y$  phase and the Sn-liquid may also have contributed to their presence at the surface of the samples. [1]

For the DSC cooled samples, the slowest cooling rate ( $0.017\text{ }^{\circ}\text{C/s}$ ) had an average  $\text{Cu}_x\text{Al}_y$  particle diameter of  $93 \pm 28\text{ }\mu\text{m}$ , while the fastest cooling rate ( $1.65\text{ }^{\circ}\text{C/s}$ ), displayed an average  $\text{Cu}_x\text{Al}_y$  particle diameter of  $31 \pm 11\text{ }\mu\text{m}$ . In comparison, the WQ sample ( $10^3\text{ }^{\circ}\text{C/s}$ ) had an average measured  $\text{Cu}_x\text{Al}_y$  particle size of  $5.4 \pm 2.4\text{ }\mu\text{m}$ . It is useful to note that although there are few particles within the DSC samples, coarsening of the particles at these slower cooling rates was apparent. The large standard deviations for the measured average  $\text{Cu}_x\text{Al}_y$  particle diameters from the DSC samples was indicative of the small number of  $\text{Cu}_x\text{Al}_y$  IMC particles found within the samples, with as few as two  $\text{Cu}_x\text{Al}_y$  particles found for the  $0.017\text{ }^{\circ}\text{C/s}$  samples. Particle size (diameter) distributions of the  $\text{Cu}_x\text{Al}_y$  phase as a function of cooling rate in Fig. 4a-e show that the distribution narrows significantly as the cooling rate increases, from  $56\text{-}133\text{ }\mu\text{m}$  for the  $0.017\text{ }^{\circ}\text{C/s}$  sample to  $1.4\text{-}17\text{ }\mu\text{m}$  for the WQ ( $10^3\text{ }^{\circ}\text{C/s}$ ) sample. The average volume fraction of the  $\text{Cu}_x\text{Al}_y$  IMC was measured within the WQ sample to be  $1.2 \pm 0.5\%$ , statistically the same as the theoretical volume fraction for  $\text{Cu}_x\text{Al}_y$  IMC of  $1.19\%$ . The  $\text{Cu}_x\text{Al}_y$  volume fractions within the DSC sample could not be accurately measured due to the small number of  $\text{Cu}_x\text{Al}_y$  particles within a given cross-sections. The morphology of the  $\text{Cu}_x\text{Al}_y$  phase for this alloy was faceted for all applied cooling rates,  $0.017\text{ }^{\circ}\text{C/s}$  to  $10^3\text{ }^{\circ}\text{C/s}$ . Figure 5a-d shows images of the deep etched composition #1 WQ sample ( $10^3\text{ }^{\circ}\text{C/s}$ ), along with qualitative EDS maps of the 2-D and 3-D surfaces of the WQ sample. In these images the distribution of Sn, Cu, and Al within the microstructure can be seen, and the association of the  $\text{Cu}_6\text{Sn}_5$  ( $\eta'$ ) phase with the surfaces of the  $\text{Cu}_x\text{Al}_y$  phase is shown.

The average  $\text{Cu}_x\text{Al}_y$  compositions measured via EDS for the DSC cooled samples indicated Cu and Al concentrations of  $66.8\text{-}68.8$  and  $31.3\text{-}33.2$  at. %, respectively, with no detectable Sn, as seen in Table II. These average  $\text{Cu}_x\text{Al}_y$  compositions are all within the  $\text{Cu}_9\text{Al}_4$  ( $\gamma_1$ ) phase field. [12] The presence of the  $\text{Cu}_9\text{Al}_4$  ( $\gamma_1$ ) phase disagrees with the calculated room temperature microstructure for this alloy composition, when omitting the ternary- $\beta$  phase formation (Fig 1d). The average  $\text{Cu}_x\text{Al}_y$  composition in the WQ sample was  $63.0$  at% Cu and  $34.4$  at. % Al, placing the WQ IMC composition within the  $\text{Cu}_{33}\text{Al}_{17}$  ( $\delta$ ) phase field. The calculated solidification path for composition #1 (Fig. 1d) predicts that the  $\text{Cu}_{33}\text{Al}_{17}$  ( $\delta$ ) phase should

be the first phase to form at ~723K (~450°C) in equilibrium with the Sn-liquid until the ternary eutectic where the alloy enters the three-phase field, i.e.,  $\text{Cu}_{33}\text{Al}_{17}$  ( $\delta$ ) +  $\text{Cu}_6\text{Sn}_5$  ( $\eta$ ) +  $\beta$ -Sn. At ~462K (~189°C) the  $\text{Cu}_6\text{Sn}_5$  ( $\eta$ ) phase is predicted to decompose into the  $\text{Cu}_6\text{Sn}_5$  ( $\eta'$ ) phase in the solid state, leaving three phase equilibrium between  $\beta$ -Sn +  $\text{Cu}_6\text{Sn}_5$  ( $\eta'$ ) +  $\text{Cu}_{33}\text{Al}_{17}$  ( $\delta$ ). The EDS composition of the  $\text{Cu}_x\text{Al}_y$  particles within the DSC samples conflicts with the predicted room temperature microstructure, but it is noted that the exact phase boundary and existence of a two-phase region between the  $\text{Cu}_9\text{Al}_4$  and  $\text{Cu}_{33}\text{Al}_{17}$  phases within the binary diagram is still under debate [12], and there is little difference that exists between the crystal structures of the two phases, primitive cubic ( $\alpha = \beta = \gamma = 90^\circ$ ) [22] and rhombohedral ( $\alpha = \beta = \gamma = 89.74^\circ$ ) [23] gamma brass structures, respectively.

For all but two  $\text{Cu}_x\text{Al}_y$  particles observed in this alloy, the Cu-Al IMC particles appeared to be single phase with convex surfaces. Two particles were observed that indicated possible decomposition of the ternary- $\beta$  phase within composition #1 in this study, but with different decomposition reactions. The 0.17 °C/s sample (Fig. 3b) showed entrapped Sn-rich regions within a  $\text{Cu}_9\text{Al}_4$  particle; in contrast, the WQ ( $10^3$  °C/s) sample showed Cu-rich regions within one observed  $\text{Cu}_{33}\text{Al}_{17}$  particle (shown in [2] in Fig. 4a). The Sn-rich regions within the  $\text{Cu}_9\text{Al}_4$  particle in the 0.17 °C/s sample had a measured EDS composition of 89.3Sn-9.6Cu at. %, with contribution of Cu signal likely from the surrounding  $\text{Cu}_9\text{Al}_4$  phase due to the small size of the Sn-rich regions. The Cu-rich regions within the  $\text{Cu}_{33}\text{Al}_{17}$  particle in the WQ ( $10^3$  °C/s) sample had an average EDS composition of 78.2Cu-20.6Al-1.0Sn at. %, close to the equilibrium composition found for the  $\alpha$  phase by Chakrabarty and Jacob [17]. There were no other observed microstructural features that indicated possible decomposition of the ternary- $\beta$  or  $\beta_1$  phases within this set of samples.

The IMC particle data for  $\text{Cu}_6\text{Sn}_5$  are also shown in Table I. The slowest DSC cooling rate of 0.017 °C/s produced the largest  $\text{Cu}_6\text{Sn}_5$  particles, with a unimodal average of  $9.1 \pm 4.8$   $\mu\text{m}$  and bimodal particle size averages of  $2.3 \pm 1.5$   $\mu\text{m}$  and  $79 \pm 37$   $\mu\text{m}$ , with the lower peak in the distribution likely representing the eutectic formation of the phase and the higher peak representing the primary formation of the phase.

The 0.17 °C/s cooling did not produce any primary Cu<sub>6</sub>Sn<sub>5</sub> within the sample cross-sections and displayed only eutectic formation with a unimodal average particle size of  $1.2 \pm 0.1 \mu\text{m}$ . The DSC cooling rates of 0.86 °C/s and 1.65 °C/s produced bimodal Cu<sub>6</sub>Sn<sub>5</sub> particle size distributions, with averages of  $1.8 \pm 1.0 \mu\text{m}$  and  $11 \pm 2.1 \mu\text{m}$ , and  $2.0 \pm 1.5 \mu\text{m}$  and  $31 \pm 17 \mu\text{m}$ , respectively. The average Cu<sub>6</sub>Sn<sub>5</sub> particle size for the WQ sample (10<sup>3</sup> °C/s) was measured at  $0.6 \pm 0.4 \mu\text{m}$ . The particle size distributions for the Cu<sub>6</sub>Sn<sub>5</sub> phase can be seen in Fig. 6a-d. It can be seen from the distributions in Fig. 6a-d that the Cu<sub>6</sub>Sn<sub>5</sub> particle size narrows as the cooling rate of the samples increases, from 0.4-245  $\mu\text{m}$  in the 0.017 °C/s sample to 0.1-3.1  $\mu\text{m}$  in the WQ (10<sup>3</sup> °C/s) sample. The average volume fraction of the Cu<sub>6</sub>Sn<sub>5</sub> phase within the WQ sample was measured at  $0.6 \pm 0.2\%$ , in good agreement with the 0.59% calculated for the theoretical volume fraction of the Cu<sub>6</sub>Sn<sub>5</sub> for this alloy at room temperature. No volume fraction values were determined for the DSC samples due to the small number of Cu<sub>6</sub>Sn<sub>5</sub> particles within the samples.

The EDS measurements from the Cu<sub>6</sub>Sn<sub>5</sub> phase within the DSC cooled samples revealed Cu and Sn concentrations ranging from 50.5-52.2 and 47.1-48.9 at. %, respectively, placing the phase composition near that of the Cu<sub>6</sub>Sn<sub>5</sub> ( $\eta'$ ) phase, but slightly Cu-poor, within the Cu<sub>6</sub>Sn<sub>5</sub> ( $\eta'$ ) +  $\beta$ -Sn two phase. The measured Cu and Sn concentrations had Cu:Sn ratios ranging from 1.03-1.11, while the Cu:Sn ratio of Cu<sub>6</sub>Sn<sub>5</sub> is 1.2. The WQ (10<sup>3</sup> °C/s) sample produced Cu<sub>6</sub>Sn<sub>5</sub> particles with average Cu and Sn concentrations of 54.4 and 45.6 at. %, respectively, with a Cu:Sn ratio of 1.19 within the Cu<sub>6</sub>Sn<sub>5</sub> ( $\eta'$ ) single phase region. Figures 5a-d illustrate the often observed formation of the Cu<sub>6</sub>Sn<sub>5</sub> particles on the surfaces of the Cu<sub>x</sub>Al<sub>y</sub> particles in the WQ (10<sup>3</sup> °C/s) sample, with the EDS maps (Fig. 5c-d) qualitatively displaying the Cu and Sn content of the Cu<sub>6</sub>Sn<sub>5</sub> particles in the WQ sample.

The aspect ratios of the Cu<sub>6</sub>Sn<sub>5</sub> particles within the DSC cooled samples, (Table I) ranged from 1.5-2.0, displaying the tendency of Cu<sub>6</sub>Sn<sub>5</sub> to form large, faceted, hollow rods along the [0001] direction. [24] When considering the formation of the Cu<sub>6</sub>Sn<sub>5</sub> phase from the ternary eutectic temperature (Fig. 1d), the observed 8-11 °C undercooling within the DSC and WQ samples would have been sufficient to promote the formation of metastable proeutectic Cu<sub>6</sub>Sn<sub>5</sub>. Given the slow cooling rates of the DSC

samples, coarsening of primary  $\text{Cu}_6\text{Sn}_5$  would also have been likely, in agreement with the room temperature DSC microstructures. In comparison to the large primary  $\text{Cu}_6\text{Sn}_5$  formation seen within the DSC samples, the  $\text{Cu}_6\text{Sn}_5$  particles within the WQ ( $10^3$  °C/s) sample were more equiaxed, with an aspect ratio of 1.3. The  $\text{Cu}_6\text{Sn}_5$  particles morphologies observed in the WQ sample using 2-D cross-sections and 3-D deep etching (Fig. 3e-g and Fig. 5a-d) were comparable: small, non-faceted, and non-hollow particle morphologies were observed, in contrast to the hollow, rod-like  $\text{Cu}_6\text{Sn}_5$  particles produced in DSC cooling treatments. There were few instances of primary, faceted  $\text{Cu}_6\text{Sn}_5$  particle formation noted in the WQ sample (see Fig. 5c). In that case, the combination of low excess Cu in the liquid after formation of the  $\text{Cu}_x\text{Al}_y$  phase (0.59 at. %) and a faster cooling rate (as compared to the DSC samples) likely resulted in limited growth of the  $\text{Cu}_6\text{Sn}_5$  phase. The faster cooling rate of the WQ sample ( $10^3$  °C/s) would have reduced the overall time in the liquid state when  $\text{Cu}_6\text{Sn}_5$  was stable, leaving little time for  $\text{Cu}_6\text{Sn}_5$  to coarsen and thus resulting in the small particle size observed in the sample ( $0.59 \pm 0.05$   $\mu\text{m}$ ), as compared to the DSC samples. The small, cylindrical  $\text{Cu}_6\text{Sn}_5$  particles seen in the deep etched sample in Fig. 5a-b support this hypothesis.

### 3.2 DA SAMPLE – COMPOSITION #2 (Sn-2.59Cu-0.43Al at. %)

Only one cooling rate ( $10^4$  °C/s) was examined for this alloy as determined by the drip atomization process. The DA sample contained a three-phase microstructure of  $\text{Cu}_x\text{Al}_y$ ,  $\text{Cu}_6\text{Sn}_5$  IMC, and  $\beta$ -Sn, as predicted from the solidification path for composition #2 (Fig. 1e). The DA particle data for  $\text{Cu}_x\text{Al}_y$  and  $\text{Cu}_6\text{Sn}_5$  phases can be found in Table I, while the compositional data for the two IMC phases can be found in Table II. The DA sample readily displayed association between  $\text{Cu}_6\text{Sn}_5$  IMC and the  $\text{Cu}_x\text{Al}_y$  particles. It can be seen from the micrographs in Fig. 7a-c that a majority of the  $\text{Cu}_6\text{Sn}_5$  formed as rods, which appear to have nucleated on faceted  $\text{Cu}_x\text{Al}_y$  IMC particles, likely with the orientation relationship  $(1\bar{2}10)_{\text{Cu}_6\text{Sn}_5} \parallel (10\bar{1})_{\text{Cu}_9\text{Al}_4}$  and  $[0001]_{\text{Cu}_6\text{Sn}_5} \parallel [111]_{\text{Cu}_9\text{Al}_4}$ , identified in [5] and [6]. The parallel rods shown in Fig. 7b and in the 3-D deep etched micrographs, the EDS map scans of the DA sample in Fig. 8a-d, and the approximately 90° angles of  $\text{Cu}_6\text{Sn}_5$  rod intersections (Fig. 8b) are consistent with growth along the  $[0001]$

direction, following nucleation and growth on the  $(10\bar{1})$  surfaces of  $\text{Cu}_x\text{Al}_y$  particles. More analysis is needed to identify the specific orientation relationships observed here for comparison with those observed previously. [5,6]

The  $\text{Cu}_x\text{Al}_y$  IMC average particle size in the DA sample ( $10^4$  °C/s) was measured at  $0.5 \pm 0.2$   $\mu\text{m}$ . As shown in Fig. 9a, the  $\text{Cu}_x\text{Al}_y$  particle distribution ranges from 0.02-2.3  $\mu\text{m}$  and possibly shows a slightly bimodal trend, with a small peak in the distribution at approximately 0.1  $\mu\text{m}$  and a larger peak at the average value of approximately 0.5  $\mu\text{m}$ . The measured volume fraction of  $\text{Cu}_x\text{Al}_y$  IMC was  $0.6 \pm 0.1$  %, a value that matches the calculated theoretical volume fraction of 0.59% for the Sn-2.59Cu-0.43Al at. % sample composition. The EDS measurements (Table II) taken from the 3-D deep etched DA sample revealed Cu and Al concentrations at an average of 67.7 and 31.9 at. %, respectively. The qualitative EDS map scans shown in Fig. 8c-d show the distribution of Sn, Cu, and Al within the DA sample microstructure and the spatial relationship between the two IMC phases,  $\text{Cu}_x\text{Al}_y$  and  $\text{Cu}_6\text{Sn}_5$ . No indications of ternary- $\beta$  phase decomposition were observed within the DA sample. The measured average  $\text{Cu}_x\text{Al}_y$  composition places the  $\text{Cu}_x\text{Al}_y$  particles within the DA sample in the  $\text{Cu}_9\text{Al}_4$  ( $\gamma_1$ ) phase. [12] The solidification path (Fig. 1e) for the DA alloy predicts a three-phase microstructure of  $\beta$ -Sn,  $\text{Cu}_6\text{Sn}_5$  ( $\eta'$ ), and  $\text{Cu}_{33}\text{Al}_{17}$  ( $\delta$ ) at room temperature. This non-equilibrium prediction conflicts with the measured EDS composition of the  $\text{Cu}_x\text{Al}_y$  particles within the sample, but as noted above, the exact phase boundary and existence of a two-phase region between the  $\text{Cu}_9\text{Al}_4$  and  $\text{Cu}_{33}\text{Al}_{17}$  phases within the binary diagram is still under debate. [12]

The average  $\text{Cu}_6\text{Sn}_5$  IMC particle size was measured at  $0.6 \pm 0.3$   $\mu\text{m}$ , with an average aspect ratio of 1.8, reflecting the elongated  $\text{Cu}_6\text{Sn}_5$  particle morphology. The particle size distribution for the  $\text{Cu}_6\text{Sn}_5$  phase within the DA ( $10^4$  °C/s) sample can be seen in Fig. 9b and ranged from 0.04-4.8  $\mu\text{m}$ . The average  $\text{Cu}_6\text{Sn}_5$  particle volume fraction within the DA sample was measured at  $1.2 \pm 0.2$  %, matching well with the theoretical volume fraction of  $\text{Cu}_6\text{Sn}_5$  calculated for the Sn-2.59Cu-0.43Al at. % sample composition of 1.22%. The EDS measurements regarding  $\text{Cu}_6\text{Sn}_5$  composition were taken from the 3-D deep etched DA sample and produced averaged Cu and Sn concentrations of 60.1 and 39.9 at. %, respectively. This resulted



in a Cu:Sn ratio of 1.5, higher than the Cu:Sn ratio of  $\text{Cu}_6\text{Sn}_5$  of 1.2. This alloy composition is within the  $\text{Cu}_3\text{Sn}$  ( $\epsilon$ ) +  $\text{Cu}_6\text{Sn}_5$  ( $\eta'$ ) two-phase field, a result that does not match the single-phase particles seen within the microstructure. The measured  $\text{Cu}_6\text{Sn}_5$  composition is approximately 3.5 at. % from the lower bound of the  $\text{Cu}_6\text{Sn}_5$  ( $\eta'$ ) single-phase region. It is possible, given the small particle size of the  $\text{Cu}_6\text{Sn}_5$  phase (0.55  $\mu\text{m}$ ), that some scattering within the measurements occurred and that the measurements were rich in Cu due to surrounding  $\text{Cu}_x\text{Al}_y$  particles.

The faceted, needle-like morphology of the  $\text{Cu}_6\text{Sn}_5$  phase within the DA sample indicates lateral, screw dislocation-assisted growth of  $\text{Cu}_6\text{Sn}_5$  prior to the ternary eutectic, previously described by Frear et al. as the mechanism for primary  $\text{Cu}_6\text{Sn}_5$  needle growth. [24] When eliminating the formation of the ternary- $\beta$  phase (Fig. 1e), the  $\text{Cu}_6\text{Sn}_5$  ( $\eta$ ) phase is found to form prior to the ternary eutectic at approximately 513K (240°C). The rapid cooling rate ( $10^4$  °C/s) of the DA sample likely restricted the overall size of the  $\text{Cu}_6\text{Sn}_5$  ( $0.6 \pm 0.3$   $\mu\text{m}$ ), while the likelihood of primary  $\text{Cu}_6\text{Sn}_5$  particle growth under non-equilibrium conditions resulted in the faceted  $\text{Cu}_6\text{Sn}_5$  rods observed within the sample. In contrast, the DSC samples with composition #1, which were predicted to require undercooling to support the formation of primary  $\text{Cu}_6\text{Sn}_5$ , displayed coarsened, faceted  $\text{Cu}_6\text{Sn}_5$  particles with hollow cores. Frear et al. examined the formation of hollow  $\text{Cu}_6\text{Sn}_5$  rods within Sn-Pb solder joints and concluded that the hollowing process occurred due to low Cu concentrations in the liquid. The liquid, having been depleted of Cu during primary  $\text{Cu}_6\text{Sn}_5$  formation, would begin to preferentially dissolve the centers of the  $\text{Cu}_6\text{Sn}_5$  rods due to the high energy of the screw dislocation cores around which the rods formed. [24] Hollow  $\text{Cu}_6\text{Sn}_5$  particles were observed in the DSC samples, likely produced due to ample time in the liquid state and low Cu concentration in the liquid (0.6 at. % after  $\text{Cu}_x\text{Al}_y$  formation). Conversely, only the beginnings of the dislocation core hollowing process were observed at the tips of the  $\text{Cu}_6\text{Sn}_5$  needles in the DA sample (Fig. 8a). The short time spent in the liquid state during DA and the higher Cu concentration in the liquid (1.7 at. % after  $\text{Cu}_x\text{Al}_y$  formation) likely limited the progression of the core hollowing process within the DA sample.

### 3.3 WQ AND MSR SAMPLES – COMPOSITION #3 (Sn-5.39Cu-1.69Al at. %)

The composition #3 WQ ( $10^3$  °C/s) and MSR samples, 5 m/s ( $10^5$  °C/s) and 25 m/s ( $10^6$  °C/s), produced three-phase microstructures of  $\beta$ -Sn,  $\text{Cu}_6\text{Sn}_5$ , and  $\text{Cu}_x\text{Al}_y$  within the as-solidified samples, as predicted by the alloy's solidification path (Fig. 1f). Micrographs of the 2-D cross-sections from the WQ and MSR samples can be seen in Fig. 10a-j and the 3-D deep etched images of the three samples can be seen in Fig. 11a-f. Particle size, distribution, volume fraction, and composition data can be found in Tables I and II. Measurements of the compositions of the  $\text{Cu}_x\text{Al}_y$  phase within the MSR samples were not performed due to the small size of the IMC particles.

The average  $\text{Cu}_x\text{Al}_y$  particle size of the WQ ( $10^3$  °C/s) sample was  $3.6 \pm 2.0$   $\mu\text{m}$ . The average  $\text{Cu}_x\text{Al}_y$  particle sizes for both MSR cooling rates 5 m/s ( $10^5$  °C/s) and 25 m/s ( $10^6$  °C/s) were  $0.1 \pm 0.1$   $\mu\text{m}$ . The similarities between the  $\text{Cu}_x\text{Al}_y$  particle size measurements for the two MSR samples indicate a possible lower limit to the apparent cooling rate induced refinement of the  $\text{Cu}_x\text{Al}_y$  phase. Additionally, the volume fractions measured for the  $\text{Cu}_x\text{Al}_y$  phase within the 2-D cross-sections of the MSR samples agree well with the theoretical volume fraction calculation for the phase based on the alloy composition. The volume fractions of  $\text{Cu}_x\text{Al}_y$  particles within the WQ ( $10^3$  °C/s), 5 m/s ( $10^5$  °C/s) MSR, and 25 m/s ( $10^6$  °C/s) MSR cooling rate samples were measured at  $2.0 \pm 0.5$  %,  $2.1 \pm 1.3$  %, and  $2.3 \pm 0.6$  %, respectively, which all agree well with the theoretical volume fraction calculation of 2.39%. Comparison of the  $\text{Cu}_x\text{Al}_y$  particle size distributions for the WQ and MSR samples can be seen in Fig. 12a-c. The distributions ranged from 1-11  $\mu\text{m}$  in the WQ ( $10^3$  °C/s) sample to 0.01-1  $\mu\text{m}$  for both MSR samples ( $10^5$  and  $10^6$  °C/s).

The average  $\text{Cu}_x\text{Al}_y$  compositions within the WQ ( $10^3$  °C/s) sample were 66.8 at% Cu and 31.6 at. % Al, (see Table II), corresponding to the  $\text{Cu}_9\text{Al}_4$  ( $\gamma_1$ ) phase. [12] The predicted phases at room temperature within the alloy included  $\beta$ -Sn,  $\text{Cu}_6\text{Sn}_5$  ( $\eta$ ), and  $\text{Cu}_{33}\text{Al}_{17}$  ( $\delta$ ) (Fig 1f). The solidification path omitting the ternary- $\beta$  phase predicted the stability of the  $\text{Cu}_{33}\text{Al}_{17}$  phase down to room temperature and the formation of the  $\text{Cu}_6\text{Sn}_5$  ( $\eta$ ) phase beginning at approximately 540K (267°C), prior to the ternary eutectic transformation. Comparison of the longitudinal and transverse wire drawing directions of the WQ ( $10^3$  °C/s)

sample (Fig. 10a-d) revealed the elongation of the IMC particles in the wire drawing direction, a microstructure not observed within the wire-drawn composition #1 WQ ( $10^3$  °C/s) sample from Section 3.1. The micrographs in Fig. 10b and 10d also show  $\text{Cu}_x\text{Al}_y$  particles with isolated pockets of Sn, a phenomenon that was noted throughout the WQ sample, possibly caused by the decomposition of the ternary- $\beta$  phase during solidification. Isolated Sn pockets were also observed in the EDS qualitative map shown in Fig. 13a. Figure 13b shows a qualitative EDS map of an area of deep etched WQ ( $10^3$  °C/s) sample where the correlations between the distributions of Sn, Cu, and Al are used to identify the individual phases.

The average  $\text{Cu}_6\text{Sn}_5$  particle sizes for the WQ ( $10^3$  °C/s), 5 m/s MSR ( $10^5$  °C/s), and 25 m/s MSR ( $10^6$  °C/s) samples were measured at  $2.5 \pm 2.0$   $\mu\text{m}$ ,  $0.5 \pm 0.4$   $\mu\text{m}$ , and  $0.3 \pm 0.2$   $\mu\text{m}$ , respectively. The particle size distributions for the  $\text{Cu}_6\text{Sn}_5$  IMC within the three Sn-5.39Cu-1.69Al at. % samples seen in Fig. 12d-f narrow with the increase in cooling rate, from 0.2-8.9  $\mu\text{m}$  in the WQ sample, 0.05-2.7  $\mu\text{m}$  in the 5 m/s MSR sample, and 0.03-2.4  $\mu\text{m}$  in the 25 m/s sample. The measured aspect ratios for the samples range from 1.5-1.6, all relatively similar, despite the morphology differences between the WQ and MSR samples. The volume fractions of the  $\text{Cu}_6\text{Sn}_5$  IMC within the three samples were measured as  $2.2 \pm 0.6$  % for the WQ sample,  $2.1 \pm 0.6$  % for the 5 m/s MSR sample, and  $1.7 \pm 0.6$  % for the 25 m/s MSR sample, as compared to the 1.90 % theoretical volume fraction for this alloy composition. The EDS measurements of the  $\text{Cu}_6\text{Sn}_5$  phase within the WQ sample revealed concentrations of 51.9 at% Cu and 47.5 at. % Sn, a composition within the  $\text{Cu}_6\text{Sn}_5$  ( $\eta'$ ) +  $\beta$ -Sn two phase field (see Table II). These Cu and Sn concentrations yield a Cu:Sn ratio of 1.1, as compared to the Cu:Sn ratio of the stoichiometric  $\text{Cu}_6\text{Sn}_5$  phase of 1.2. The high Sn concentration in the  $\text{Cu}_6\text{Sn}_5$  particle may be due to acquired signal contributed by the surrounding Sn matrix phase. The range of  $\text{Cu}_6\text{Sn}_5$  IMC compositions within the deep etched 5 m/s and 25 m/s MSR microstructures ( $10^5$  °C/s and  $10^6$  °C/s) via EDS were 42.1-46.8 at. % Cu, 43.7-47.6 at. % Sn, and 9.5-10.3 at. % Al. This result was unexpected and it is quite possible that the Al concentration is attributed to the measurements from the surrounding  $\text{Cu}_x\text{Al}_y$  phase and/or  $\text{Cu}_x\text{Al}_y$  particles entrapped within the  $\text{Cu}_6\text{Sn}_5$

particles (as seen in Fig. 10i-j). This ternary composition could also indicate incomplete decomposition of the ternary- $\beta$  phase in the solid state due to the high solidification rates within the samples.

The WQ sample displayed faceted  $\text{Cu}_6\text{Sn}_5$  particle formation, with some particles displaying the hollow core morphology (Fig. 10d and 11a). Given that  $\text{Cu}_6\text{Sn}_5$  is predicted to form below approximately 540K (267°C), primary, faceted  $\text{Cu}_6\text{Sn}_5$  particles would be expected to appear within the room temperature microstructure. The  $\text{Cu}_6\text{Sn}_5$  particles appear to nucleate on the  $\text{Cu}_x\text{Al}_y$  particles, as seen in Fig. 10b. This type of configuration suggests a possible epitaxial orientation relationship between  $\text{Cu}_6\text{Sn}_5$  and  $\text{Cu}_x\text{Al}_y$ , as reported in [5] and [6], but it is not as pronounced as observed in the DA morphology. The only morphology of  $\text{Cu}_6\text{Sn}_5$  particles observed within the WQ sample was large, faceted rods, with no bi-modal particle size distribution observed.

The cross-sections of the MSR samples shown in Fig. 10e-j show the distributions and morphologies of the  $\text{Cu}_x\text{Al}_y$  and  $\text{Cu}_6\text{Sn}_5$  phases for the two different cooling rates. Regions containing large, elliptical, non-faceted  $\text{Cu}_6\text{Sn}_5$  particles were noted throughout the MSR samples (Figs. 10i-j), along with regions containing significantly smaller, non-faceted particles. The morphological transition of the  $\text{Cu}_6\text{Sn}_5$  from faceted rods in the WQ sample to non-faceted elliptical particles with a bimodal particle size distribution in the MSR samples is likely due to the high cooling rates for the MSR samples,  $10^5$  °C/s and  $10^6$  °C/s. Despite the remaining Cu in the liquid expected after  $\text{Cu}_x\text{Al}_y$  formation (2.1 at. % Cu), the short time in the liquid state during  $\text{Cu}_6\text{Sn}_5$  formation and particle coarsening precluded the transition to faceted rods. The deep-etched MSR samples shown in Fig. 11c-f also displayed bimodal IMC particle distributions, with some relatively large particles and many others that had particle sizes on the nano-scale. Due to their small particle sizes, compositional measurements on the nano-scale particle phase could not be performed to distinguish  $\text{Cu}_x\text{Al}_y$  from  $\text{Cu}_6\text{Sn}_5$ . Given the accuracy of the measured volume fractions of the  $\text{Cu}_x\text{Al}_y$  phase within the MSR samples and the predicted high transformation temperature of the  $\text{Cu}_{33}\text{Al}_{17}$  phase, first solidifying at ~813K (~540°C) and completely transformed by 573K (~300°C) (Fig. 1f), it is unlikely that all of these nano-scale particles are that of the  $\text{Cu}_x\text{Al}_y$  phase. When further referencing the solidification

path without the ternary- $\beta$  phase in Fig. 1f, it can be seen that the mole fraction of the  $\text{Cu}_6\text{Sn}_5$  phase more than doubles at the alloy's eutectic transformation temperature. Given this increase in  $\text{Cu}_6\text{Sn}_5$  phase fraction at the eutectic temperature and the extremely rapid cooling rates of the MSR samples, it is likely that the nano-scale particles in Fig. 11d and 11f are predominantly  $\text{Cu}_6\text{Sn}_5$  formed from the eutectic transformation; but TEM analysis would be required for confirmation.

To summarize the IMC particle size measurements made for all compositions, the graphs in Fig. 14a-b illustrate the overall refinement of the  $\text{Cu}_x\text{Al}_y$  and  $\text{Cu}_6\text{Sn}_5$  particle sizes for the range of the applied cooling rate techniques. Figure 14a-b displays the progression from the slowest controlled cooling at  $0.017^\circ\text{C/s}$  to the fastest RSP method employed via melt spinning at a wheel speed of 25 m/s (estimated cooling rate of  $10^6$   $^\circ\text{C/s}$ ), which resulted in an overall decrease in  $\text{Cu}_x\text{Al}_y$  and  $\text{Cu}_6\text{Sn}_5$  particle sizes by approximately two orders of magnitude. These data illustrate the ability to manipulate the as-solidified particle sizes of the  $\text{Cu}_x\text{Al}_y$  and  $\text{Cu}_6\text{Sn}_5$  IMC based solely on the chosen solidification method. Secondly, the data show that there is strong microstructural evidence for the  $\text{Cu}_6\text{Sn}_5$  IMC particles nucleating on  $\text{Cu}_x\text{Al}_y$  particles only at intermediate cooling rates, as observed for the WQ and DA samples. However, there is less direct (EDS reveals a high Al content in the apparent  $\text{Cu}_6\text{Sn}_5$  particles) evidence in both MSR samples of  $\text{Cu}_6\text{Sn}_5$  particles nucleating on (embedded, unseen)  $\text{Cu}_x\text{Al}_y$  particles, but the SEM resolution was not sufficient to observe this. In addition, faceted rod formation and the subsequent hollowing of  $\text{Cu}_6\text{Sn}_5$  rods is shown to depend on composition and cooling rate. For example, the slowly cooled DSC samples displayed faceted, hollow  $\text{Cu}_6\text{Sn}_5$  due to low Cu concentrations in the liquid during solidification and the slow cooling rate of the samples, while the WQ sample of the same composition displayed non-faceted, non-hollow  $\text{Cu}_6\text{Sn}_5$  particles with the increase in cooling rate, as outlined in Table I. The combination of these results suggests that a cooling rate regime utilizing water quenching to drip atomization ( $10^3$   $^\circ\text{C/s}$  -  $10^4$   $^\circ\text{C/s}$ ) is ideal to achieve IMC particle refinement while simultaneously maintaining the  $\text{Cu}_x\text{Al}_y/\text{Cu}_6\text{Sn}_5$  nucleant relationship during initial solidification from the melt. Finally, there appears to be little microstructural evidence for the presence of the ternary- $\beta$  phase during

solidification or for its decomposition at lower temperatures for the DSC cooled, DA, WQ, or MSR samples. (The specific instances of microstructures that suggested decomposition of the ternary- $\beta$  phase were described here, but were rare.) This result is in contrast to what was observed previously for WQ Sn-Ag-Cu-Al quaternary alloys [2], suggesting that the ternary- $\beta$  phase does not form within the ternary alloy composition ranges and cooling rates investigated here and may be unstable, in agreement with observations by Xian et al. for a different set of Sn-Cu-Al alloys. [5,6]

It is widely recognized that the  $\text{Cu}_6\text{Sn}_5$  particle size distribution can be strongly affected by variations in  $\beta$ -Sn undercooling during alloy solidification. These often unpredictable and unrepeatable variations in  $\beta$ -Sn undercooling can lead to increased  $\text{Cu}_6\text{Sn}_5$  particle size with increased  $\beta$ -Sn undercooling. [25] In Part II of this study, the coarsening behavior of alloys during thermal reflow cycling between 293 – 523 K (20 – 250 °C) for 1 to 5 cycles for the DA and 5 m/s MSR samples was examined. It was shown that the particle size of the  $\text{Cu}_x\text{Al}_y$  was essentially unaffected by the thermal cycling, displaying no signs of coarsening during reflow cycling. In contrast, the particle size distribution of the  $\text{Cu}_6\text{Sn}_5$  phase at the slow cooling rates used in Part II during reflow cycling (10°C/min or 0.17°C/s) varied quite significantly corresponding to the large variations in  $\beta$ -Sn undercoolings observed. Such a large range in particle size distribution of the  $\text{Cu}_6\text{Sn}_5$  phase was not observed in the samples from Part I of this study, and it is because of this that the authors are confident that the changes in cooling rate are the dominating factor in the refinement of the as-solidified IMC microstructures. Additionally, the high diffusivity of Cu in Sn certainly means that these intermetallics could potentially change over time at room temperature. [25] Room temperature microstructural evolution has been reported for  $\text{Cu}_6\text{Sn}_5$  in many different solder systems, but the authors have not observed any room temperature microstructural changes in regards to the  $\text{Cu}_x\text{Al}_y$  phase in this study and believe the phase to be quite stable at room temperature, especially considering the results from Part II of this study, where the particle size of the  $\text{Cu}_x\text{Al}_y$  was essentially unaffected by the thermal cycling to 523 K (250°C).

#### 4. CONCLUSIONS

This paper has shown that the  $\text{Cu}_x\text{Al}_y$  and  $\text{Cu}_6\text{Sn}_5$  IMC particle formations within Sn-Cu-Al alloys are highly dependent on alloy composition and cooling rate. Through application of RSP methods, with cooling rates up to approximately  $10^6$  °C/s, the particle sizes and particle size distributions of the  $\text{Cu}_x\text{Al}_y$  and  $\text{Cu}_6\text{Sn}_5$  IMC particle phases were refined well into the sub-micron range. For application of the fastest cooling rate of  $10^6$  °C/s, produced via melt spinning of composition #3 at a 25m/s wheel speed, the average  $\text{Cu}_x\text{Al}_y$  IMC particle diameter was refined to  $0.1 \pm 0.1$   $\mu\text{m}$ , while the  $\text{Cu}_6\text{Sn}_5$  particle size was refined to  $0.3 \pm 0.2$   $\mu\text{m}$ .

The morphology of the  $\text{Cu}_6\text{Sn}_5$  phase within the Sn-Cu-Al solders was also manipulated via the use of RSP. A transition in the  $\text{Cu}_6\text{Sn}_5$  morphology from faceted rods to non-faceted, more equiaxed particles occurred with increased cooling rates, with the cooling rate threshold dependent on composition, i.e. dependent on available Cu content within the liquid during cooling and, therefore, on the formation temperature of the  $\text{Cu}_6\text{Sn}_5$  phase (predicted in Fig. 1d-f). This transition for composition #1 occurred with increased cooling rate from DSC cooling (maximum of 1.65 °C/s) to WQ processing ( $10^3$  °C/s). When considering composition #1, the  $\text{Cu}_6\text{Sn}_5$  phase was not predicted to form until the ternary eutectic reaction at ~500K (~227°C) (Fig. 1d). Due to the low Cu content in the liquid (0.59 at. %) after the complete formation of the  $\text{Cu}_x\text{Al}_y$  phase, the formation of any primary  $\text{Cu}_6\text{Sn}_5$  within composition #1 would have required undercooling below the ternary reaction. The cooling rate threshold for composition #1 was therefore lower than that of composition #3, due to the latter alloy's increased content of Cu in the liquid (2.1 at. % Cu), where formation of the  $\text{Cu}_6\text{Sn}_5$  phase was predicted to begin at ~540K (~267°C) (Fig. 1f). The faceted to non-faceted transition in  $\text{Cu}_6\text{Sn}_5$  was observed within composition #3 between the WQ cooling rate ( $10^3$  °C/s) and the MSR processing at  $10^5$  °C/s. The DA sample (composition #2,  $10^4$  °C/s) displayed faceted  $\text{Cu}_6\text{Sn}_5$  formation, but there were no other tested cooling rates for this sample composition with which to compare.

Finally, the room temperature microstructures revealed little evidence of ternary- $\beta$  phase formation during solidification, or its decomposition at lower temperatures, within all of the current ternary alloy

compositions and cooling rates. (The few instances of microstructures that suggested possible decomposition of the ternary- $\beta$  phase were described, but it is noted that these instances were rare.) Based on these observations, solidification path predictions omitting the ternary- $\beta$  phase formation were calculated and presented. The predicted solidification paths all displayed the stabilization of the  $\text{Cu}_{33}\text{Al}_{17}$  ( $\delta$ ) phase down to room temperature, with the  $\text{Cu}_6\text{Sn}_5$  ( $\eta$ ) phase forming at various temperatures: at the eutectic temperature ( $\sim 500\text{K}$  ( $\sim 227^\circ\text{C}$ )) for composition #1, but higher than the ternary eutectic for the composition #2 (at  $\sim 513\text{K}$  ( $\sim 240^\circ\text{C}$ )) and composition #3 (at  $\sim 540\text{K}$  ( $\sim 267^\circ\text{C}$ )). This is in contrast to what was observed previously for WQ Sn-Ag-Cu-Al quaternary alloys, where the microstructures showed multiple, interconnected IMC phases within single particles. [2] In this study, the absence of such structures suggests that the ternary- $\beta$  phase did not form within the ternary alloy composition ranges and cooling rates investigated here and may, in fact, be unstable, in agreement with observations by Xian et al. for a different set of Sn-Cu-Al alloys. [5,6] Continued research into the ranges of stability of the ternary- $\beta$  phase should be explored via long-term isothermal annealing and quenching experiments on select Sn-rich Sn-Cu-Al ternary alloys.

In general, these experiments show strong evidence for the nucleation of  $\text{Cu}_6\text{Sn}_5$  on  $\text{Cu}_x\text{Al}_y$  particles at different cooling rates and compositions and, therefore, that  $\text{Cu}_x\text{Al}_y$  particles can be effective nucleation agents when the average particle sizes decrease and size distributions of the IMCs narrow with increasing cooling rates. It was determined that to achieve a microstructure with both  $\text{Cu}_x\text{Al}_y$  and  $\text{Cu}_6\text{Sn}_5$  IMC refinement and a maintained  $\text{Cu}_x\text{Al}_y/\text{Cu}_6\text{Sn}_5$  nucleant relationship, cooling rates within the range of water quenching to drip atomization ( $10^3\text{ }^\circ\text{C/s} - 10^4\text{ }^\circ\text{C/s}$ ) are the most effective. The usefulness of these alloys in controlling microstructure evolution in solder interconnects will depend on the continued ability of the  $\text{Cu}_x\text{Al}_y$  particles to be effective nucleating agents for  $\text{Cu}_6\text{Sn}_5$  during multiple reflow cycles. In Part II, the melting and solidification behaviors of the Sn-2.59Cu-0.43Al at. % DA ( $10^4\text{ }^\circ\text{C/s}$ ) alloy and the Sn-5.39Cu-1.69Al at. % 5 m/s ( $10^5\text{ }^\circ\text{C/s}$ ) MSR alloy were examined using DSC temperature cycling (293K - 523K



(20°C - 250°C)) up to 5 reflow cycles to study the nucleation and coarsening behavior of the  $\text{Cu}_x\text{Al}_y$  and  $\text{Cu}_6\text{Sn}_5$  IMC phases present within both alloys. [21]

## ACKNOWLEDGEMENTS

This work was supported by Ames Laboratory, Purdue University, and Nihon Superior through Ames Lab contract No.DE-AC02-07CH11358. Additionally, this research was conducted with government support under and awarded by DoD, Air Force Office of Scientific Research, National Defense Science and Engineering Graduate (NDSEG) Fellowship, 32 CFR 168a. The research group is grateful for the support and helpful communications provided by Nihon Superior, and for the assistance of Fukuda Co. in producing the drip atomized solder sample presented in this paper. The group would also like to thank Kevin Dennis (dennis@ameslab.gov) of Ames Laboratory for help in producing the DSC cooled and melt spun ribbon alloys, Warren Straszheim (wesaia@iastate.edu) of Iowa State University's MARL microscopy facility for assistance and expertise in the use of the field emission SEM, and John Holaday (jholaday@purdue.edu) of Purdue University for calculating the Thermo-Calc solidification paths presented.

## REFERENCES

- [1] A.J. Boesenberg, I.E. Anderson, and J.L. Harringa: *J. Electron. Mater.*, 2012, vol. 41, pp. 1868–81.
- [2] K.N. Reeve, I.E. Anderson, and C.A. Handwerker: *J. Electron. Mater.*, 2015, vol. 44, pp. 842–66.
- [3] S.D. McDonald, K. Nogita, J. Read, T. Ventura, and T. Nishimura: *J. Electron. Mater.*, 2012, vol. 42, pp. 256–62.
- [4] K. Sweatman, T. Nishimura, S.D. McDonald, M. Whitewick, and K. Nogita: *SMT Mag.*, 2014, pp. 30–40.
- [5] J.W. Xian, S.A. Belyakov, T.B. Britton, and C.M. Gourlay: *J. Alloys Compd.*, 2015, vol. 619, pp. 345–55.
- [6] J.W. Xian, S.A. Belyakov, and C.M. Gourlay: *J. Electron. Mater.*, 2015, vol. 45, pp. 69–78.
- [7] C.S. Smith, W.E. Lindief, and W. Conn: *Trans. Am. Inst. Min. Metall. Eng.*, 1933, vol. 104, pp. 69–105.
- [8] G. Wasserman: *Metallwirtschaft*, 1934, vol. 13, pp. 133–39.
- [9] J L Murray: *Int. Met. Rev.*, 1985, vol. 30, pp. 211–33.
- [10] X.J. Liu, I. Ohnuma, R. Kainuma, and K. Ishida: *J. Alloys Compd.*, 1998, vol. 264, pp. 201–8.
- [11] H. Okamoto: *Desk Handbook: Phase Diagrams for Binary Alloys*, ASM International, Materials Park, Columbus, OH, USA, 2000.
- [12] N. Ponweiser, C.L. Lengauer, and K.W. Richter: *Intermetallics*, 2011, vol. 19, pp. 1737–46.
- [13] S. Fürtauer, D. Li, D. Cupid, and H. Flandorfer: *Intermetallics*, 2013, vol. 34, pp. 142–47.
- [14] D. Li, P. Franke, S. Fürtauer, D. Cupid, and H. Flandorfer: *Intermetallics*, 2013, vol. 34, pp. 148–58.
- [15] J.S.L. Leach and G.V. Raynor: *Proc. R. Soc.*, 1954, vol. 224, pp. 251–59.
- [16] A.K. Chakrabarty and K.T. Jacob: *Int. J. Mater. Res.*, 2013, vol. 104, pp. 430–41.

- 636 [17] A.K. Chakrabarty and K.T. Jacob: *J. Phase Equilibria Diffus.*, 2013, vol. 34, pp. 267–76.
- 637 [18] D. Mirković, J. Gröbner, and R. Schmid-Fetzer: *Mater. Sci. Eng. A*, 2008, vol. 487, pp. 456–67.
- 638 [19] W.J. Boettinger and J.H. Perepezko: in *Rapidly Solidified Cryst. Alloy.*, S.K. Das, B.H. Kear, and  
639 C.M. Adam, eds., The Metallurgical Society, Inc., Warrendale, PA, USA, 1985, pp. 21–58.
- 640 [20] S.A. Belyakov and C.M. Gourlay: *Acta Mater.*, 2014, vol. 71, pp. 56–68.
- 641 [21] K. N. Reeve, S. M. Choquette, I. E. Anderson, and C. A. Handwerker: *Metall. Mater. Trans. A*,  
642 under review, 2016.
- 643 [22] L. Arnberg and S. Westman: *Acta Crystallogr. Sect. A*, 1978, vol. 34, pp. 399–404.
- 644 [23] E.H. Kisi and J.D. Browne: *Acta Crystallogr. Sect. B Struct. Sci.*, 1991, vol. 47, pp. 835–43.
- 645 [24] D. Frear, D. Grivas, and J.W. Jr. Morris: *J. Electron. Mater.*, 1987, vol. 16, pp. 181–86.
- 646 [25] B.F. Dyson, T.R. Anthony, and D. Turnbull: *J. Appl. Phys.*, 1967, vol. 38, p. 3408.
- 647
- 648

## FIGURE CAPTIONS

Figure 1: Predicted alloy solidification paths (A-C) with the ternary- $\beta$  formation and (D-F) without the ternary- $\beta$  phase formation for all alloy compositions produced via Thermo-Calc<sup>1</sup> TCSLD1. The y-axis of each diagram is magnified to show the transitions of the IMC phases at 0-0.1 mole fraction. (Color figures available online).

<sup>1</sup> <http://www.thermocalc.com/start/> - Thermo-Calc Software, Stockholm, Sweden.

Figure 2: A projection of the Sn-Cu-Al ternary liquidus surface. The presented figure has been adapted from Mirković et al. and orthogonally displays the Sn-rich corner of the ternary such that the transitions of the labeled sample compositions can be viewed. [18] (Color figures available online).

Figure 3: Backscatter electron (BSE) SEM micrographs of the solder microstructures for the (A-D) DSC and (E-G) WQ composition #1 samples. The black contrast particles are  $\text{Cu}_x\text{Al}_y$  IMC, the dark grey contrast particles and areas are  $\text{Cu}_6\text{Sn}_5$  IMC, and the light grey matrix is  $\beta$ -Sn. In (a-d), the black border along the  $\beta$ -Sn matrix is the edge of the DSC solder samples. (Color figures available online).

Figure 4: (A-E)  $\text{Cu}_x\text{Al}_y$  IMC particle size distributions for composition #1 DSC and WQ cooling rate samples. The y-axis shows the number fraction of  $\text{Cu}_x\text{Al}_y$  particle (bars; left axes), as well as the cumulative distribution function (lines; right axes). The x-axis plots the  $\text{Cu}_x\text{Al}_y$  IMC particle size.

Figure 5: (A-B) SEM secondary electron (SE) images of regions of Sn-2.29Cu-0.86Al at. % WQ sample after deep etching to reveal the 3-D structure of the IMC within the alloy. (C) SEM EDS map scan of a 2-D cross-section of the Sn-2.29Cu-0.86Al at. % WQ sample taken in BSE mode, and (D) SEM EDS map of a 3-D structure of the Sn-2.29Cu-0.86Al at. % WQ sample after deep etching taken in SE mode. Association between the  $\text{Cu}_6\text{Sn}_5$  (light grey) and  $\text{Cu}_x\text{Al}_y$  (BSE=black, SE=dark grey) particle phases can be seen throughout the micrographs. (Color figures available online).

Figure 6: (A-E)  $\text{Cu}_6\text{Sn}_5$  IMC particle size distributions for the Sn-2.29Cu-0.86Al at. % DSC and WQ cooling rate samples. The y-axis show the number fraction of  $\text{Cu}_6\text{Sn}_5$  particles (bars, left axes) as well as the cumulative distribution function (lines, right axes). The x-axis plots the  $\text{Cu}_6\text{Sn}_5$  IMC particle size in log scale for 0.1-1000  $\mu\text{m}$ . (Color figures available online).

Figure 7: (A-C) BSE SEM micrographs of the solder microstructure for DA Sn-2.59Cu-0.43Al at. % sample ( $10^4$  °C/s). The black contrast particles are  $\text{Cu}_x\text{Al}_y$  IMC, the dark grey contrast particles and areas are  $\text{Cu}_6\text{Sn}_5$  IMC, and the light grey matrix is  $\beta$ -Sn.

Figure 8: (A-B) SEM SE images of regions of the Sn-2.59Cu-0.43Al at. % DA ( $10^4$  °C/s) sample after deep etching to reveal the 3-D structure of the IMC within the alloy. (C-D) SEM EDS map scans of the 3-D structure of the Sn-2.59Cu-0.43Al at. % DA sample. Association between the  $\text{Cu}_6\text{Sn}_5$  and  $\text{Cu}_x\text{Al}_y$  particle phases can be seen. (Color figures available online).

Figure 9: IMC particle size distributions for the Sn-2.59Cu-0.43Al at. % DA ( $10^4$  °C/s) sample for the (A)  $\text{Cu}_x\text{Al}_y$  IMC particle phase and (B) the  $\text{Cu}_6\text{Sn}_5$  IMC particle phase. The y-axis shows the number fraction of particles (bars, left axes) as well as the cumulative distribution function (lines, right axes). The x-axis plots the IMC particle size from 0-5  $\mu\text{m}$ .

Figure 10: BSE SEM micrographs of the solder microstructure for Sn-5.39Cu-1.69Al at. % samples, (A-D) WQ ( $10^3$  °C/s) sample, (E-G) 5 m/s MSR ( $10^5$  °C/s) sample, and (H-J) 25 m/s MSR ( $10^6$  °C/s) sample. The black contrast particles are  $\text{Cu}_x\text{Al}_y$  IMC, the dark grey contrast particles and areas are  $\text{Cu}_6\text{Sn}_5$  IMC, and the light grey matrix is  $\beta$ -Sn. (Color figures available online).

Figure 11: SEM (A-F) SE images of the Sn-5.39Cu-1.69Al at. % samples after deep etching to reveal the 3-D structure of the IMC within the alloy. (A-B) WQ ( $10^3$  °C/s) sample, (C-D) 5 m/s MSR ( $10^5$  °C/s) sample, and (E-F) 25 m/s MSR ( $10^6$  °C/s) sample. Association between the  $\text{Cu}_6\text{Sn}_5$  (light grey) and  $\text{Cu}_x\text{Al}_y$  (dark grey) particle phases can be seen in (A-B). Extreme refinement of the IMC can be seen in (C-F). (Color figures available online).

Figure 12: IMC particle size distributions for the Sn-5.39Cu-1.69Al at. % samples for the (A-C)  $\text{Cu}_x\text{Al}_y$  IMC particles within the WQ ( $10^3$  °C/s), 5 m/s MSR ( $10^5$  °C/s), and 25 m/s MSR ( $10^6$  °C/s), respectively, and (D-F) the  $\text{Cu}_6\text{Sn}_5$  IMC particles within the WQ ( $10^3$  °C/s), 5 m/s MSR ( $10^5$  °C/s), and 25 m/s MSR ( $10^6$  °C/s), respectively. Insets are used in (B) and (C) to display the distribution of  $\text{Cu}_x\text{Al}_y$  within the MSR samples from 0-1  $\mu\text{m}$ , and in (E) and (F) to display the trailing ends of each  $\text{Cu}_6\text{Sn}_5$  distribution.

Figure 13: SEM BSE images and EDS map scans of regions of Sn-5.39Cu-0.86Al at. % WQ ( $10^3$  °C/s) sample (A) 2-D cross-section and (B) SE images after deep etching to reveal the 3-D structure of the IMC within the alloy. Association between the  $\text{Cu}_6\text{Sn}_5$  (light grey) and  $\text{Cu}_x\text{Al}_y$  (black) particle phases can be seen throughout the micrographs. Sn-entrapment within the  $\text{Cu}_x\text{Al}_y$  phase is also observed in (A). (Color figures available online).

Figure 14: Graph of (A)  $\text{Cu}_x\text{Al}_y$  and (B)  $\text{Cu}_6\text{Sn}_5$  IMC average particle diameters versus applied estimated cooling rate for the three alloy compositions examined. In (B), the average unimodal and bimodal particle diameters for the DSC cooled samples are given. The linear fits shown in (A) and (B) portray the decreasing size of the  $\text{Cu}_x\text{Al}_y$  and  $\text{Cu}_6\text{Sn}_5$  particles with applied cooling rate for the corresponding alloy compositions. (Color figures available online).

Table I: The cooling methods, estimated cooling rates, sample compositions, Cu<sub>x</sub>Al<sub>y</sub> particle data, and Cu<sub>6</sub>Sn<sub>5</sub> particle data for all samples.

Cooling Method	Estimated Cooling Rate (°C/s)	Sample Composition (at. %)			Cu <sub>x</sub> Al <sub>y</sub> Particle Data					Cu <sub>6</sub> Sn <sub>5</sub> Particle Data								Morphology
		Sn	Cu	Al	Unimodal Avg. Dia. (μm)	Max. Dia. (μm)	Min. Dia. (μm)	Avg. Vol. %	Calc. Vol. %	Unimodal Avg. Dia. (μm)	Bimodal Avg. Dia. (μm)		Max Dia. (μm)	Min Dia. (μm)	Avg. Aspect Ratios	Avg. Vol. %	Calc. Vol %	
DSC	0.017	96.84	2.29	0.86	93 ± 28	133	56	--	1.19	9.1 ± 4.8	2.3 ± 1.5	79 ± 37†	245	0.4	1.7 ± 0.9	--	0.59	Faceted (hollow core)
DSC	0.17	96.84	2.29	0.86	60 ± 15	84	27	--	1.19	1.2 ± 0.1	--	--	8.9	0.4	1.5 ± 0.6	--	0.59	--
DSC	0.83	96.84	2.29	0.86	39 ± 7.4	53	23	--	1.19	2.7 ± 2.1	1.8 ± 1.0	11 ± 2.1	56	0.4	1.8 ± 1.1	--	0.59	Faceted (hollow core)
DSC	1.65	96.84	2.29	0.86	31 ± 11	52	10	--	1.19	4.8 ± 3.1	2.0 ± 1.5	31 ± 17	132	0.4	2.0 ± 1.2	--	0.59	Faceted (hollow core)
WQ	10 <sup>3</sup>	96.84	2.29	0.86	5.4 ± 2.4	17	1.4	1.2 ± 0.5	1.19	0.6 ± 0.4	--	--	3.1	0.1	1.3 ± 0.4	0.6 ± 0.2	0.59	Non-Faceted
DA	10 <sup>4</sup>	96.97	2.59	0.43	0.5 ± 0.2	2.3	0.02	0.6 ± 0.1	0.59	0.6 ± 0.3	--	--	4.8	0.04	1.8 ± 1.2	1.2 ± 0.2	1.22	Faceted (start of hollow core)
WQ	10 <sup>3</sup>	92.92	5.39	1.69	3.6 ± 2.0	11	1.0	2.0 ± 0.5	2.39	2.5 ± 2.0	--	--	8.9	0.2	1.5 ± 0.5	2.2 ± 0.6	1.90	Faceted (hollow core)
MSR	10 <sup>5</sup>	92.92	5.39	1.69	0.1 ± 0.1	1.0	0.01	2.1 ± 1.3	2.39	0.5 ± 0.4	--	--	2.7	0.05	1.6 ± 0.7	2.1 ± 0.6	1.90	Non-Faceted
MSR	10 <sup>6</sup>	92.92	5.39	1.69	0.1 ± 0.1	0.8	0.01	2.3 ± 0.6	2.39	0.3 ± 0.2	--	--	2.4	0.03	1.5 ± 0.5	1.7 ± 0.6	1.90	Non-Faceted
† Single outlier excluded (245 μm) from calculation of average and standard deviation																		

Table II: Measured EDS compositions for the  $\text{Cu}_x\text{Al}_y$  and  $\text{Cu}_6\text{Sn}_5$  phases found within the Sn-Cu-Al solder samples. Accurate compositional measurement of the  $\text{Cu}_6\text{Sn}_5$  within the 0.17 °C/s sample cross-sections could not be made without the influence of the surrounding Sn matrix, and the  $\text{Cu}_x\text{Al}_y$  particle size within the MSR samples were too small for accurate EDS measurement (EDS spot size = 1  $\mu\text{m}$ ).

Cooling Method	Est. Cooling Rate (°C/s)	Sample Compositions			EDS on $\text{Cu}_x\text{Al}_y$		EDS on $\text{Cu}_6\text{Sn}_5$		
		Sn	Cu	Al	Cu	Al	Cu	Sn	Al
DSC	0.017	96.84	2.29	0.86	68.1	32.0	52.2	47.1	--
DSC	0.17	96.84	2.29	0.86	66.8	33.2	--	--	--
DSC	0.83	96.84	2.29	0.86	68.8	31.3	50.6	48.7	--
DSC	1.65	96.84	2.29	0.86	67.5	32.4	50.5	48.9	--
WQ	$10^3$	96.84	2.29	0.86	63.0	34.4	54.4	45.6	--
DA	$10^4$	96.97	2.59	0.43	67.7	31.9	60.1	39.9	--
WQ	$10^3$	92.92	5.39	1.69	66.8	31.6	51.9	47.5	--
MSR	$10^5$	92.92	5.39	1.69	--	--	46.8	43.7	9.5
MSR	$10^6$	92.92	5.39	1.69	--	--	42.1	47.6	10.3

*\*All values are given in units of atomic percent (at. %), unless otherwise stated.*



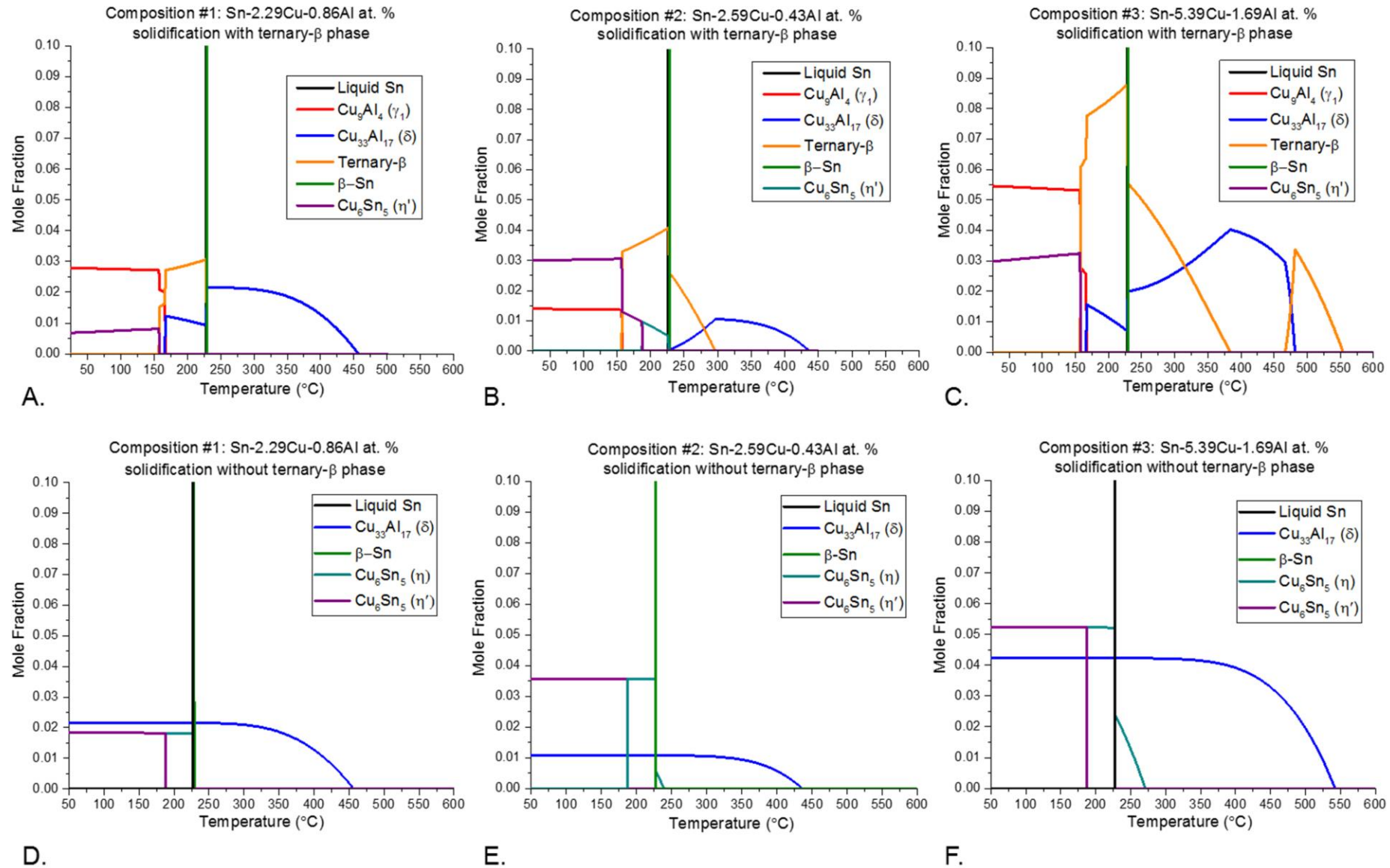


Figure 1: Predicted alloy solidification paths (A-C) with the ternary-β formation and (D-F) without the ternary-β phase formation for all alloy compositions produced via Thermo-Calc<sup>1</sup> TCSD1. The y-axis of each diagram is magnified to show the transitions of the IMC phases at 0-0.1 mole fraction. (Color figures available online).

<sup>1</sup> <http://www.thermocalc.com/start/> - Thermo-Calc Software, Stockholm, Sweden.

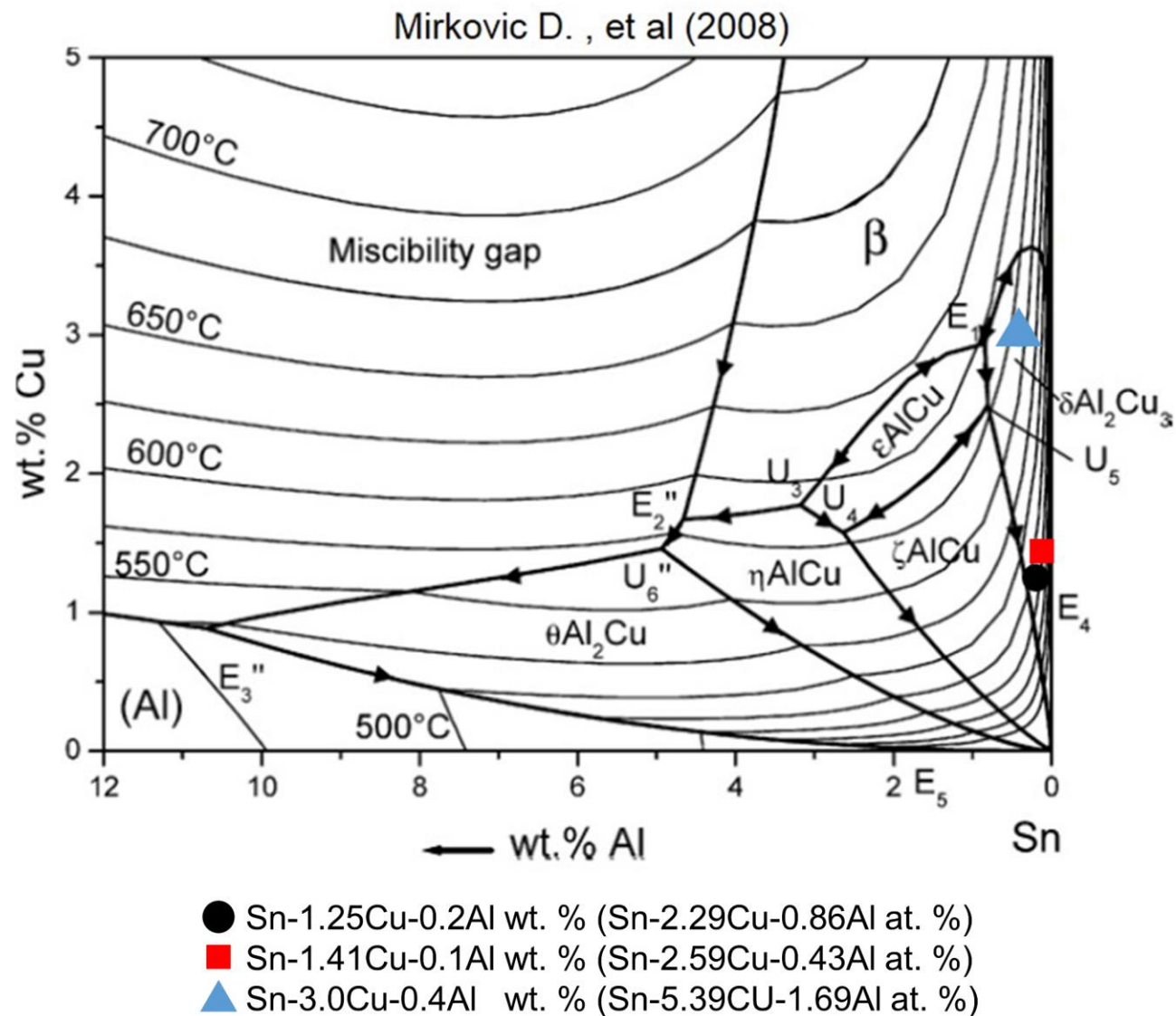


Figure 2: The Sn-Cu-Al ternary liquidus projection computed by Mirković et al. in 2008. [18] The liquidus projection is orthogonally portrayed from the Sn-rich corner, such that the transitions of the labeled sample compositions can be viewed. (Color figures available online).

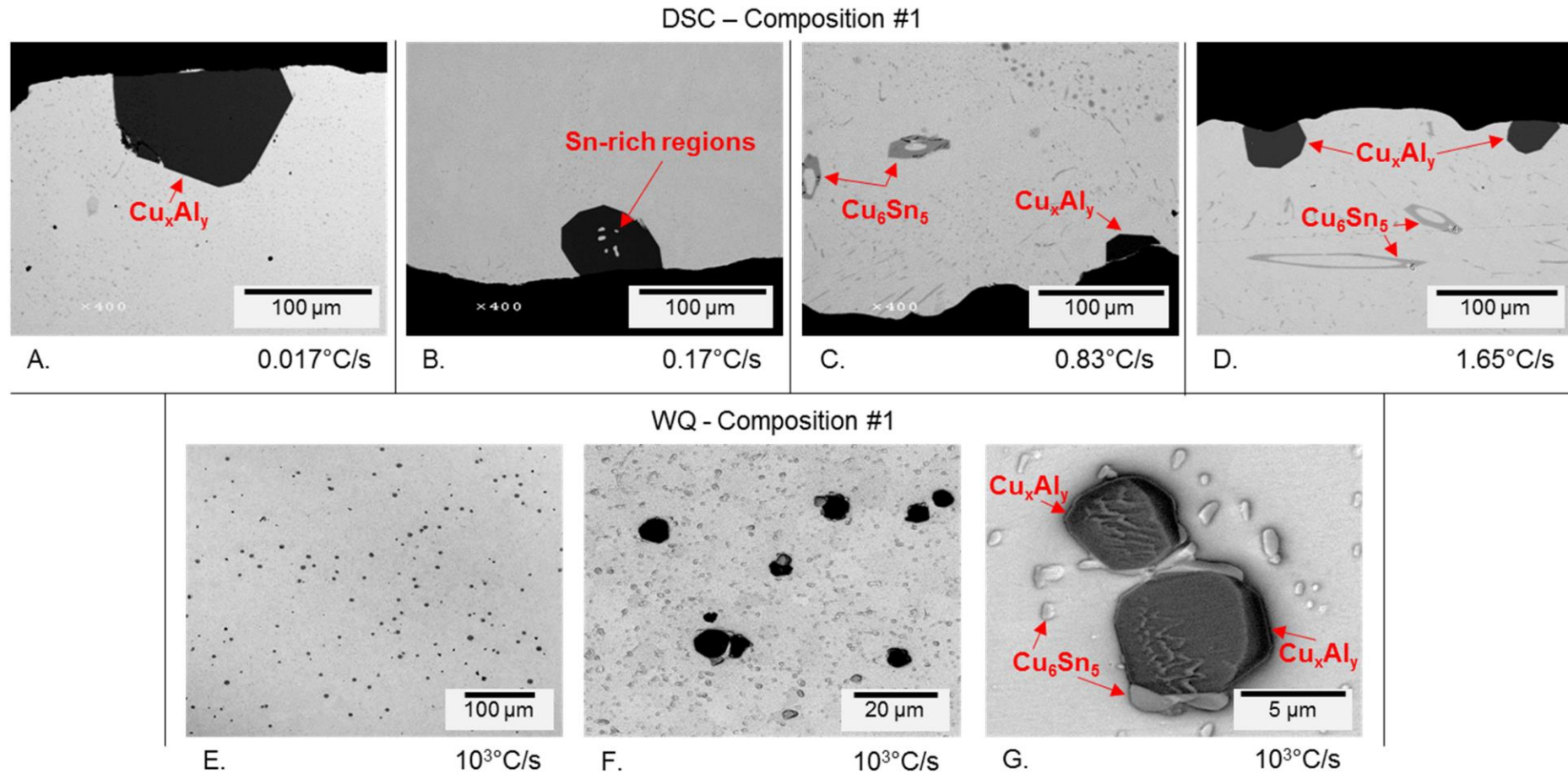


Figure 3: Backscatter electron (BSE) SEM micrographs of the solder microstructures for the (A-D) DSC and (E-G) WQ composition #1 samples. The black contrast particle are  $\text{Cu}_x\text{Al}_y$  IMC, the dark grey contrast particles and areas are  $\text{Cu}_6\text{Sn}_5$  IMC, and the light grey matrix is  $\beta\text{-Sn}$ . In (a-d), the black border along the  $\beta\text{-Sn}$  matrix is the edge of the DSC solder samples. (Color figures available online).

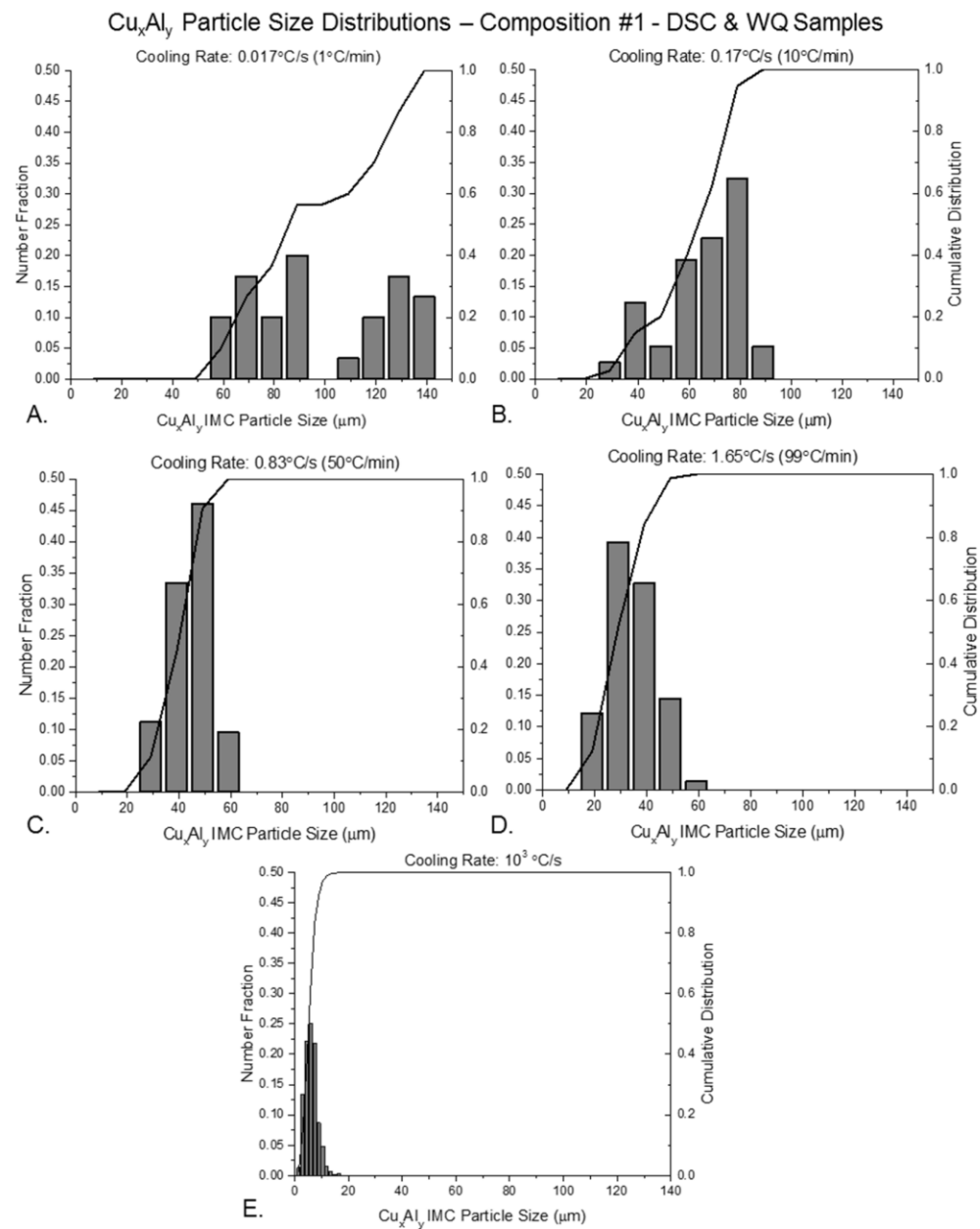


Figure 4: (A-E)  $\text{Cu}_x\text{Al}_y$  IMC particle size distributions for composition #1 DSC and WQ cooling rate samples. The y-axis shows the number fraction of  $\text{Cu}_x\text{Al}_y$  particle (bars; left axes), as well as the cumulative distribution function (lines; right axes). The x-axis plots the  $\text{Cu}_x\text{Al}_y$  IMC particle size.



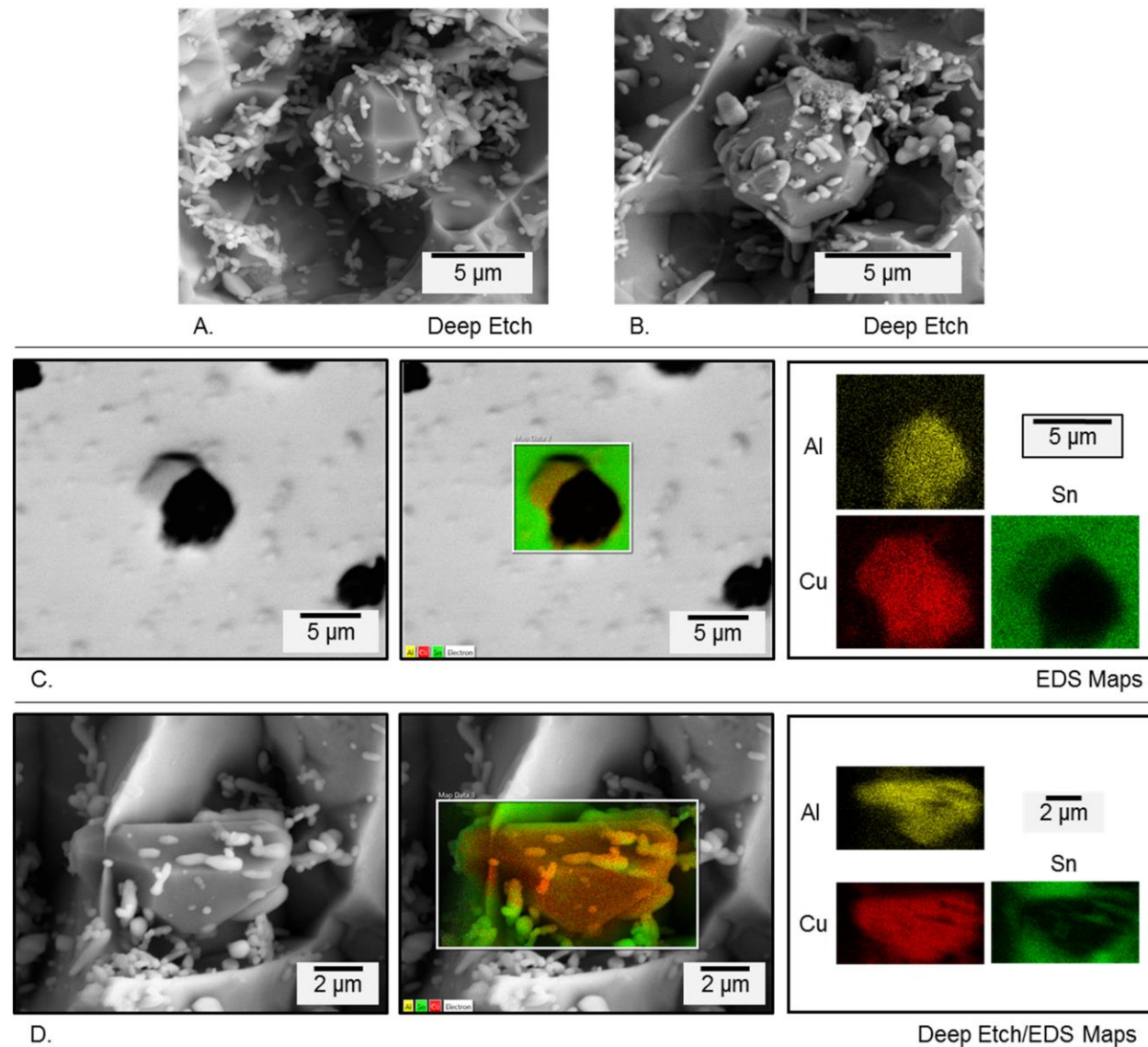


Figure 5: (A-B) SEM secondary electron (SE) images of regions of Sn-2.29Cu-0.86Al at. % WQ sample after deep etching to reveal the 3-D structure of the IMC within the alloy. (C) SEM EDS map scan of a 2-D cross-section of the Sn-2.29Cu-0.86Al at. % WQ sample taken in BSE mode, and (D) SEM EDS map of a 3-D structure of the Sn-2.29Cu-0.86Al at. % WQ sample after deep etching taken in SE mode. Association between the  $\text{Cu}_6\text{Sn}_5$  (light grey) and  $\text{Cu}_x\text{Al}_y$  (BSE=black, SE=dark grey) particle phases can be seen throughout the micrographs. (Color figures available online).

$\text{Cu}_6\text{Sn}_5$  Particle Size Distributions – Composition #1 - DSC & WQ Samples

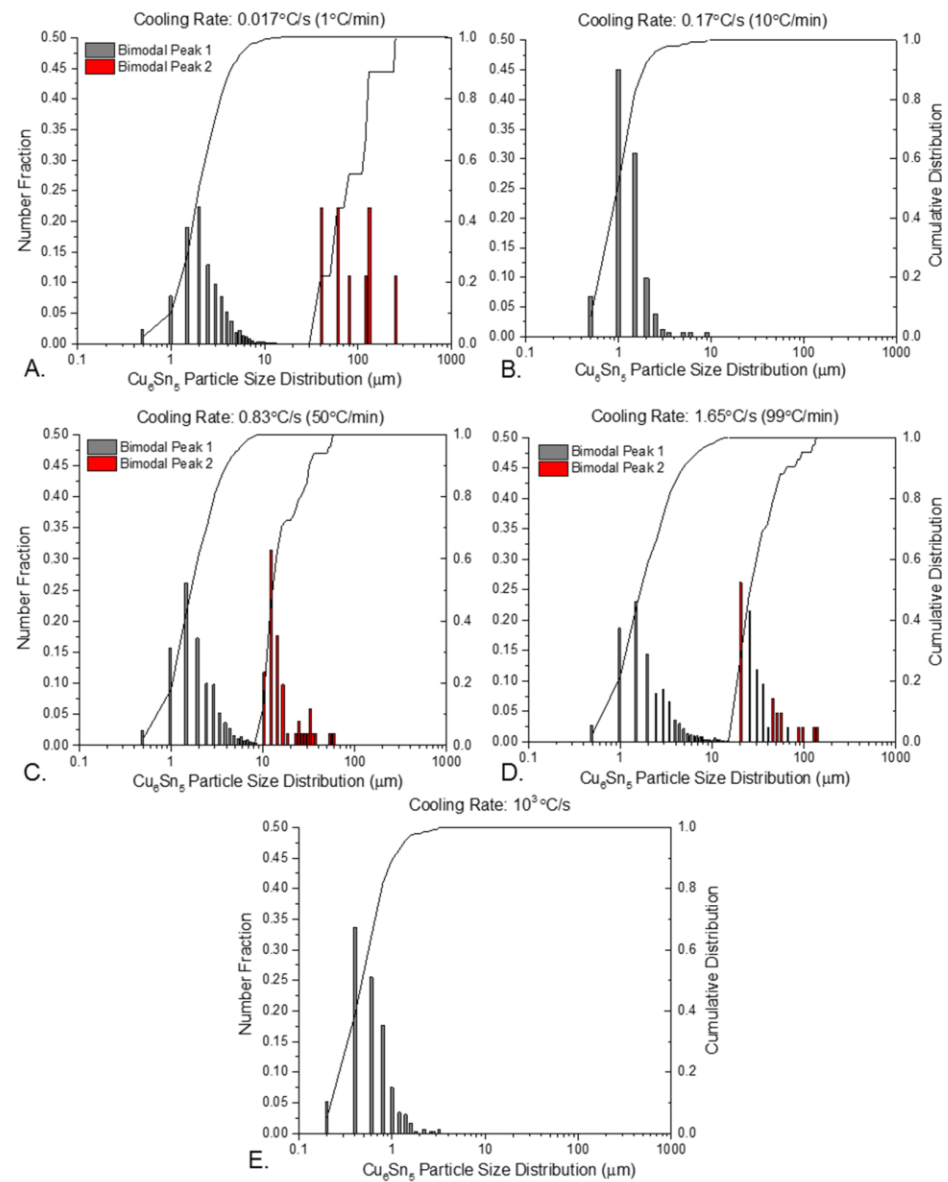
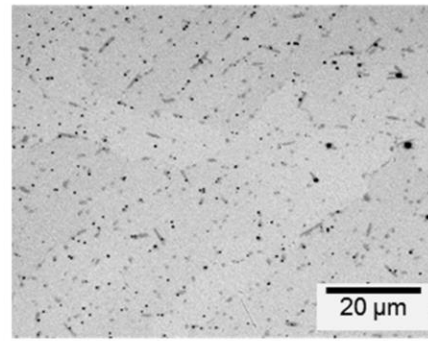
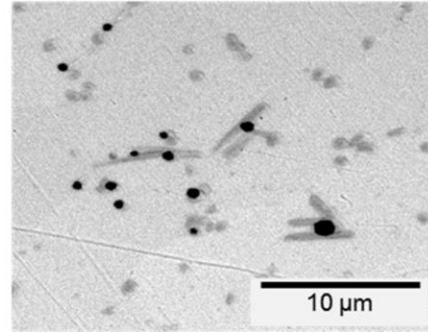


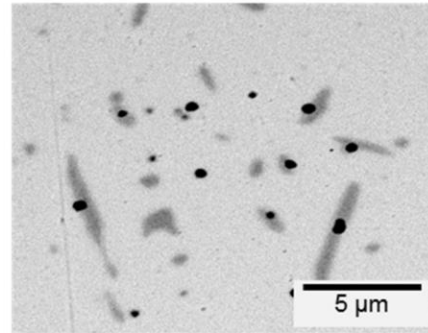
Figure 6: (A-E)  $\text{Cu}_6\text{Sn}_5$  IMC particle size distributions for the Sn-2.29Cu-0.86Al at. % DSC and WQ cooling rate samples. The y-axis show the number fraction of  $\text{Cu}_6\text{Sn}_5$  particles (bars, left axes) as well as the cumulative distribution function (lines, right axes). The x-axis plots the  $\text{Cu}_6\text{Sn}_5$  IMC particle size in log scale for 0.1-1000  $\mu\text{m}$ . (Color figures available online).



A.  $10^4\text{°C/s}$



B.  $10^4\text{°C/s}$



C.  $10^4\text{°C/s}$

Figure 7: (A-C) BSE SEM micrographs of the solder microstructure for DA Sn-2.59Cu-0.43Al at. % sample ( $10^4\text{°C/s}$ ). The black contrast particles are  $\text{Cu}_x\text{Al}_y$  IMC, the dark grey contrast particles and areas are  $\text{Cu}_6\text{Sn}_5$  IMC, and the light grey matrix is  $\beta\text{-Sn}$ .

DA - Composition #2

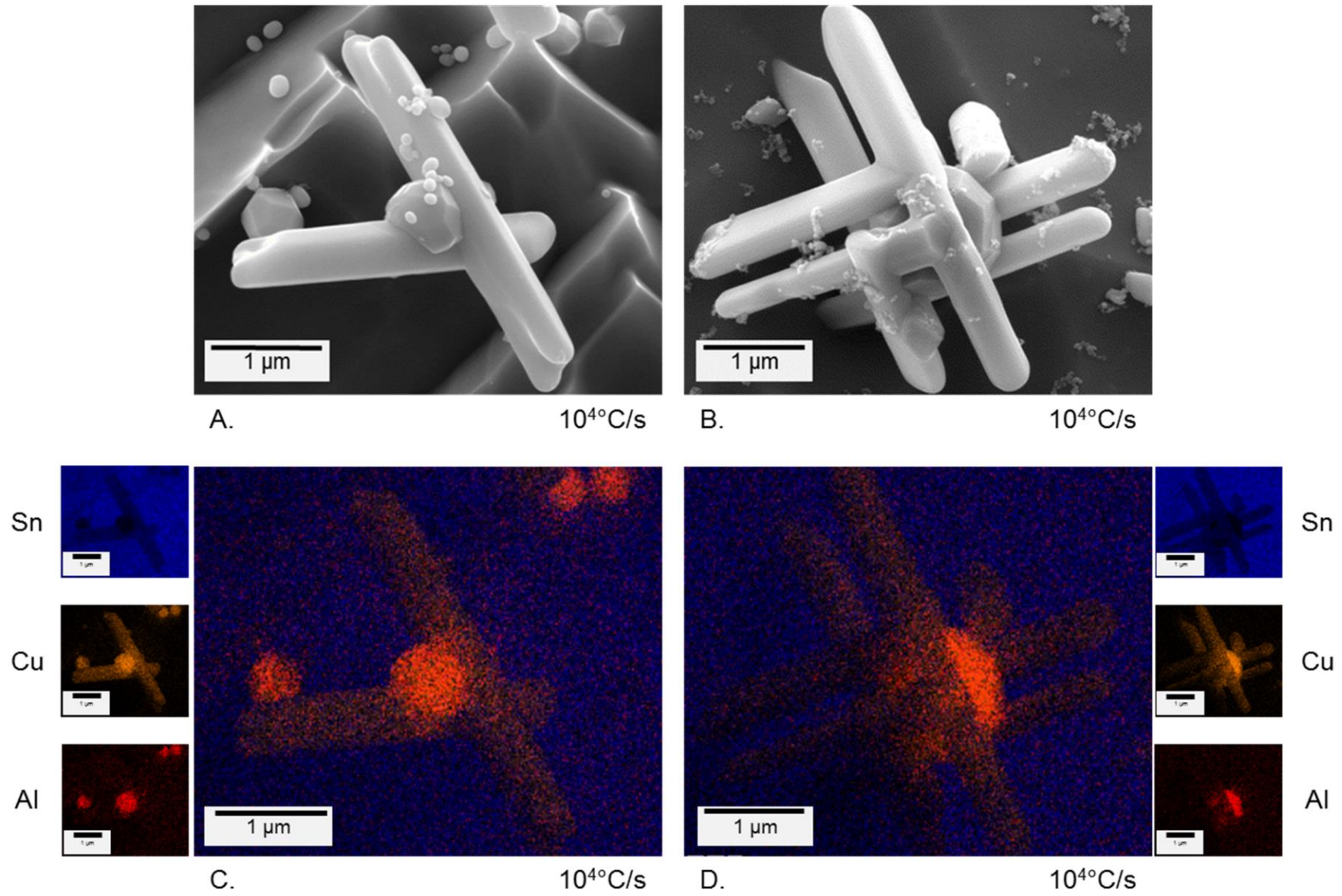
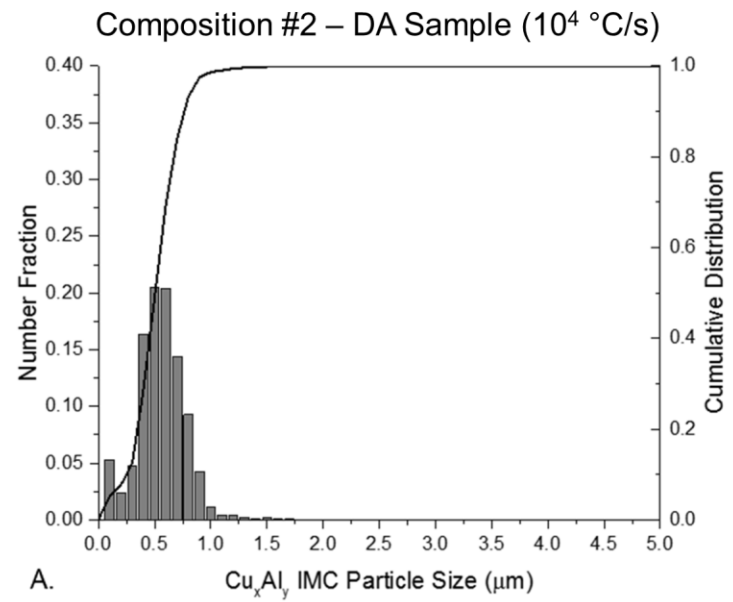
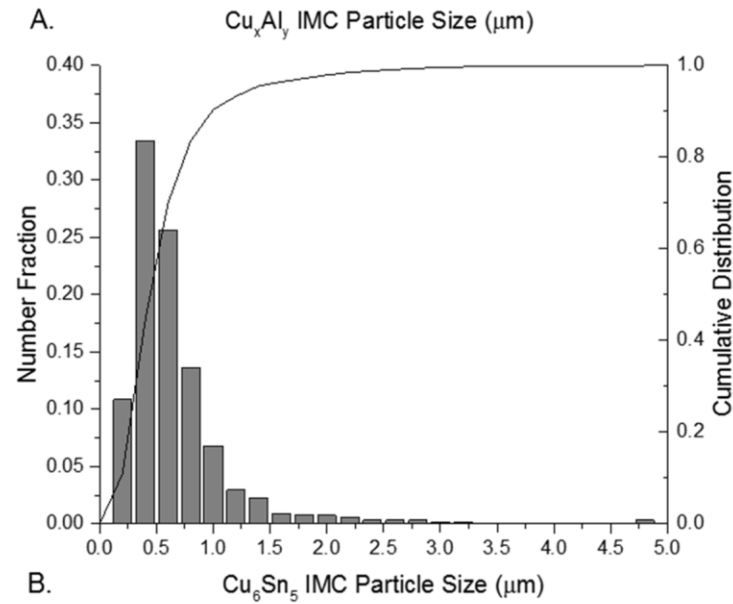


Figure 8: (A-B) SEM secondary electron (SE) images of regions of the Sn-2.59Cu-0.43Al at. % DA ( $10^4$  °C/s) sample after deep etching to reveal the 3-D structure of the IMC within the alloy. (C-D) SEM EDS map scans of the 3-D structure of the Sn-2.59Cu-0.43Al at. % DA sample. Association between the  $\text{Cu}_6\text{Sn}_5$  and  $\text{Cu}_x\text{Al}_y$  particle phases can be seen. (Color figures available online).





A.



B.

Figure 9: IMC particle size distributions for the Sn-2.59Cu-0.43Al at. % DA ( $10^4$  °C/s) sample for the (A)  $\text{Cu}_x\text{Al}_y$  IMC particle phase and (B) the  $\text{Cu}_6\text{Sn}_5$  IMC particle phase. The y-axis shows the number fraction of particles (bars, left axes) as well as the cumulative distribution function (lines, right axes). The x-axis plots the IMC particle size from 0-5  $\mu\text{m}$ .

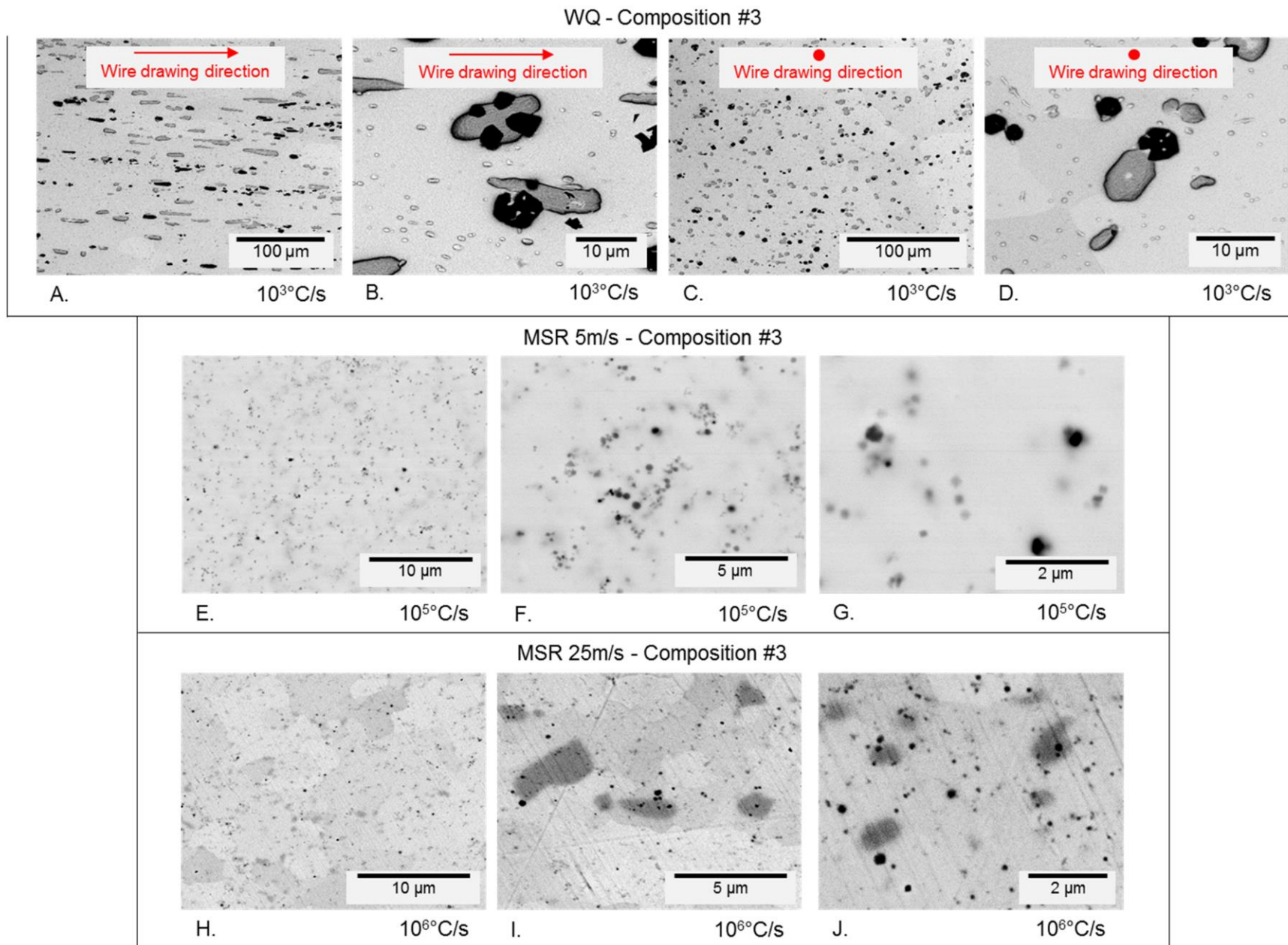
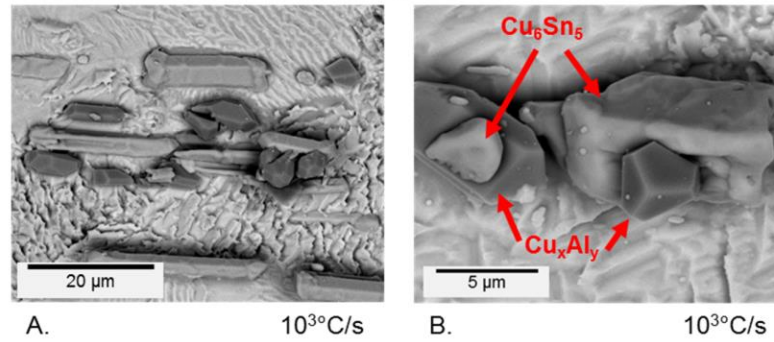
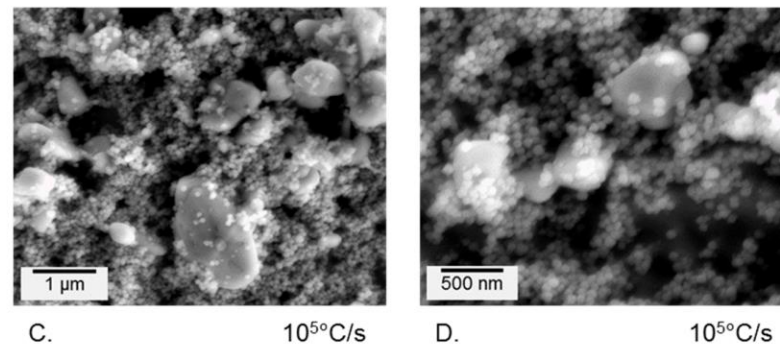


Figure 10: BSE SEM micrographs of the solder microstructure for Sn-5.39Cu-1.69Al at. % samples, (A-D) WQ ( $10^3\text{°C/s}$ ) sample, (E-G) 5 m/s MSR ( $10^5\text{°C/s}$ ) sample, and (H-J) 25 m/s MSR ( $10^6\text{°C/s}$ ) sample. The black contrast particles are  $\text{Cu}_x\text{Al}_y$  IMC, the dark grey contrast particles and areas are  $\text{Cu}_6\text{Sn}_5$  IMC, and the light grey matrix is  $\beta\text{-Sn}$ . (Color figures available online).

WQ - Composition #3



MSR 5m/s - Composition #3



MSR 25m/s - Composition #3

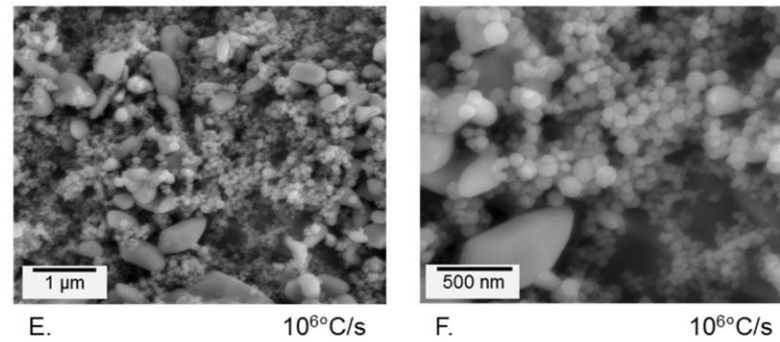
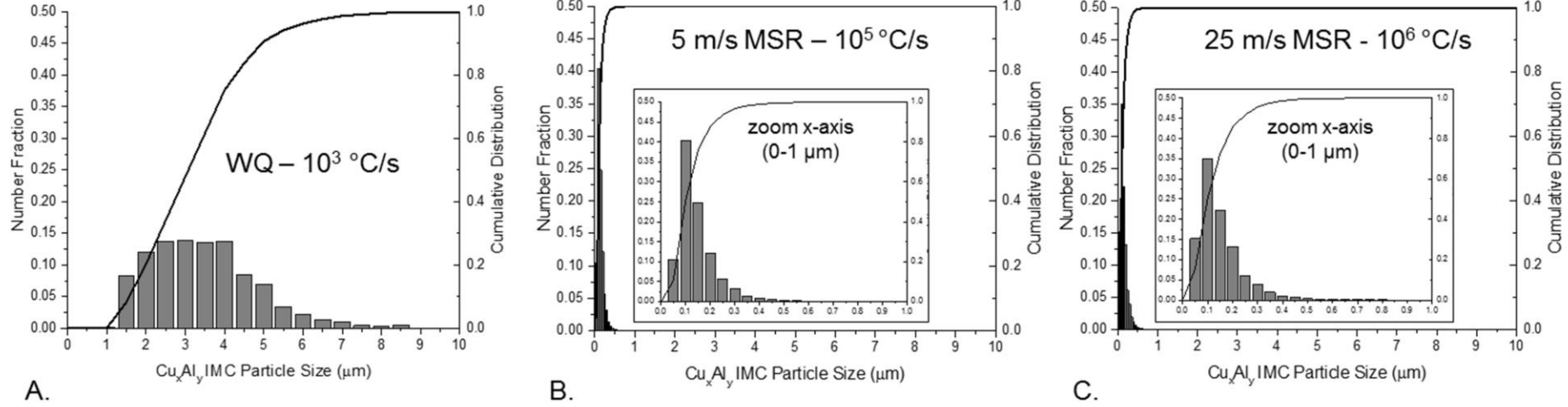


Figure 11: SEM (A-F) SE images of the Sn-5.39Cu-1.69Al at. % samples after deep etching to reveal the 3-D structure of the IMC within the alloy. (A-B) WQ ( $10^3$  °C/s) sample, (C-D) 5 m/s MSR ( $10^5$  °C/s) sample, and (E-F) 25 m/s MSR ( $10^6$  °C/s) sample. Association between the  $\text{Cu}_6\text{Sn}_5$  (light grey) and  $\text{CuAl}_3$  (dark grey) particle phases can be seen in (A-B). Extreme refinement of the IMC can be seen in (C-F). (Color figures available online).

### $\text{Cu}_x\text{Al}_y$ IMC Particle Size Distributions – Composition #3 - WQ & MSR



### $\text{Cu}_6\text{Sn}_5$ IMC Particle Size Distributions – Composition #3 - WQ & MSR

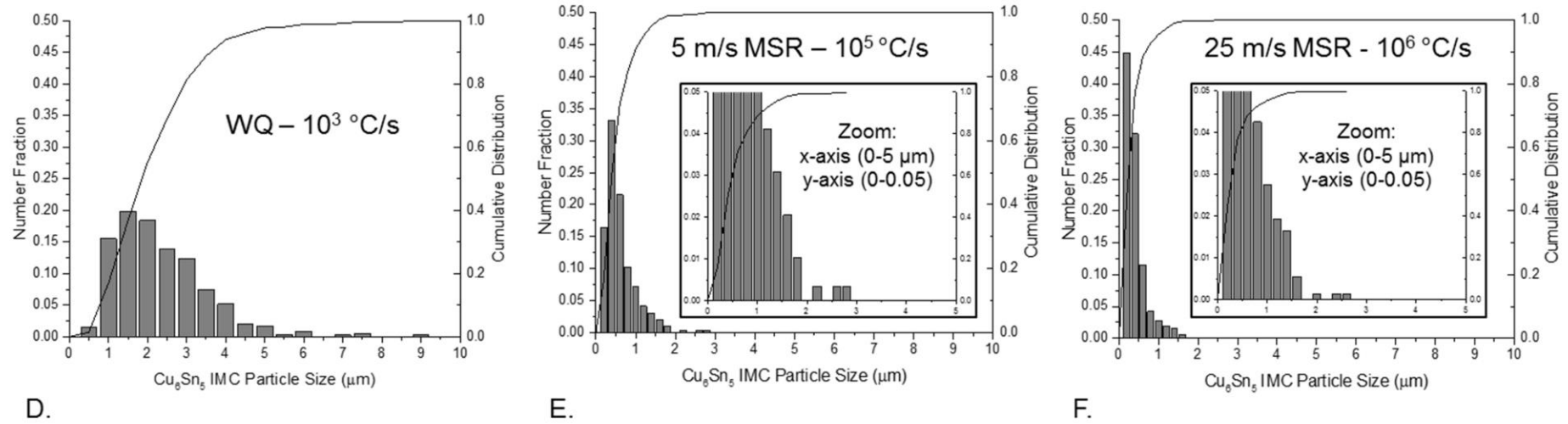
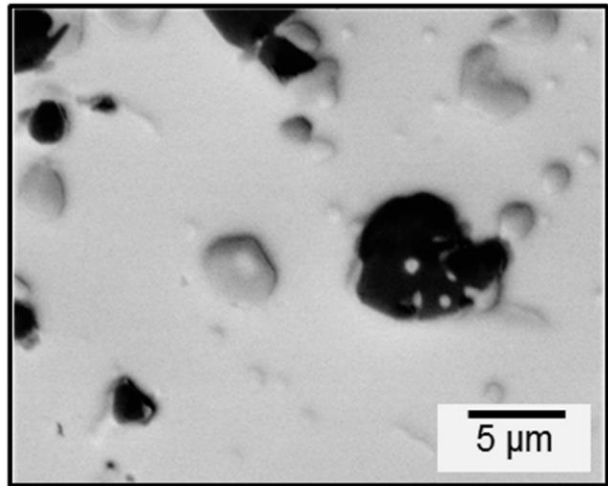


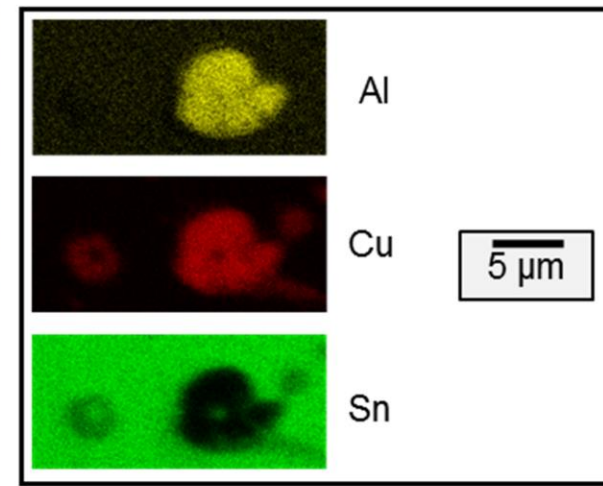
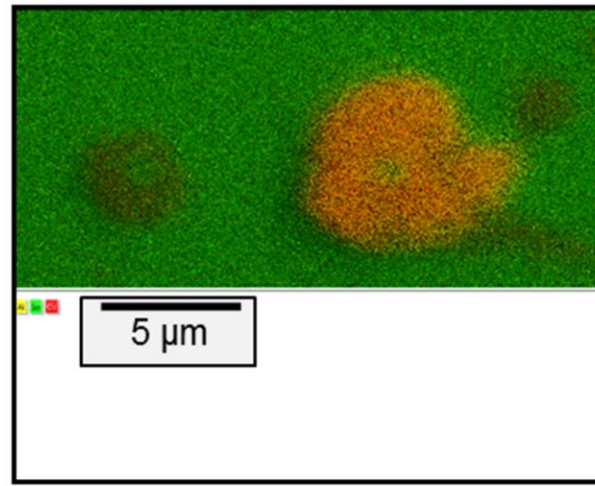
Figure 12: IMC particle size distributions for the Sn-5.39Cu-1.69Al at. % samples for the (A-C)  $\text{Cu}_x\text{Al}_y$  IMC particles within the WQ ( $10^3$  °C/s), 5 m/s MSR ( $10^5$  °C/s), and 25 m/s MSR ( $10^6$  °C/s), respectively, and (D-F) the  $\text{Cu}_6\text{Sn}_5$  IMC particles within the WQ ( $10^3$  °C/s), 5 m/s MSR ( $10^5$  °C/s), and 25 m/s MSR ( $10^6$  °C/s), respectively. Insets are used in (B) and (C) to display the distribution of  $\text{Cu}_x\text{Al}_y$  within the MSR samples from 0-1  $\mu\text{m}$ , and in (E) and (F) to display the trailing ends of each  $\text{Cu}_6\text{Sn}_5$  distribution.



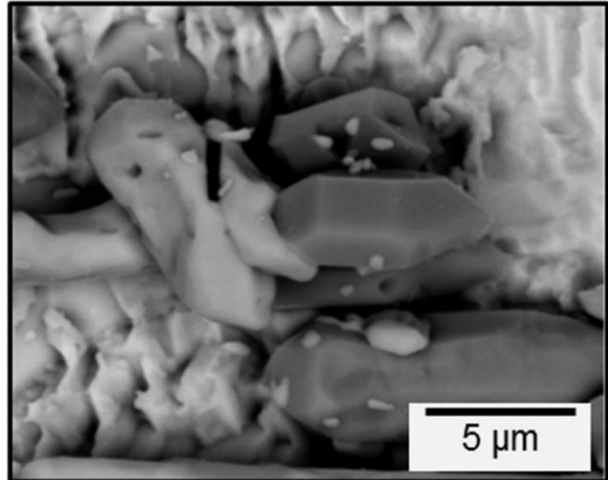
# WQ – Composition#3



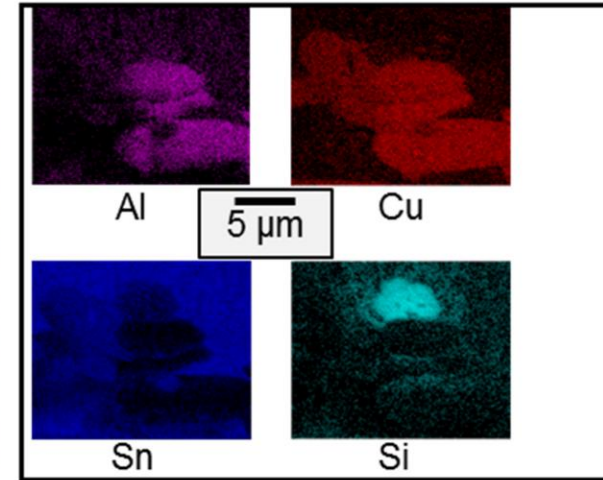
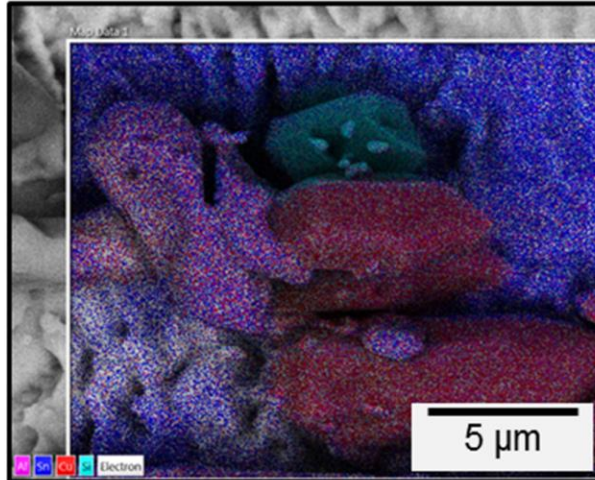
A.



EDS Maps



B.



Deep Etch/EDS Maps

Figure 13: SEM BSE images and EDS map scans of regions of Sn-5.39Cu-0.86Al at. % WQ ( $10^3$  °C/s) sample (A) 2-D cross-section and (B) SE images after deep etching to reveal the 3-D structure of the IMC within the alloy. Association between the  $\text{Cu}_6\text{Sn}_5$  (light grey) and  $\text{Cu}_x\text{Al}_y$  (black) particle phases can be seen throughout the micrographs. Sn-entrapment within the  $\text{Cu}_x\text{Al}_y$  phase is also observed in (A). (Color figures available online).

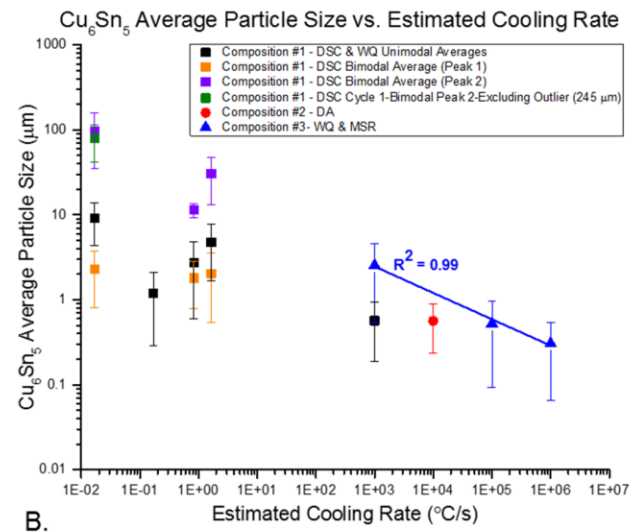
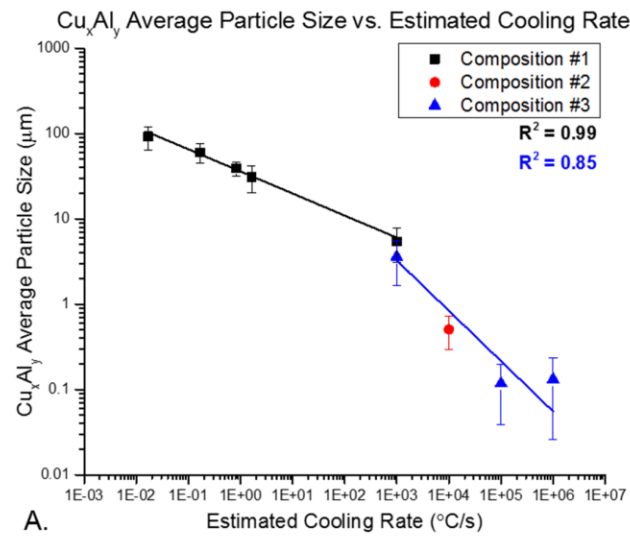


Figure 14: Graph of (A)  $\text{Cu}_x\text{Al}_y$  and (B)  $\text{Cu}_6\text{Sn}_5$  IMC average particle diameters versus applied estimated cooling rate for the three alloy compositions examined. In (B), the average unimodal and bimodal particle diameters for the DSC cooled samples are given. The linear fits shown in (A) and (B) portray the decreasing size of the  $\text{Cu}_x\text{Al}_y$  and  $\text{Cu}_6\text{Sn}_5$  particles with applied cooling rate for the corresponding alloy compositions. (Color figures available online).